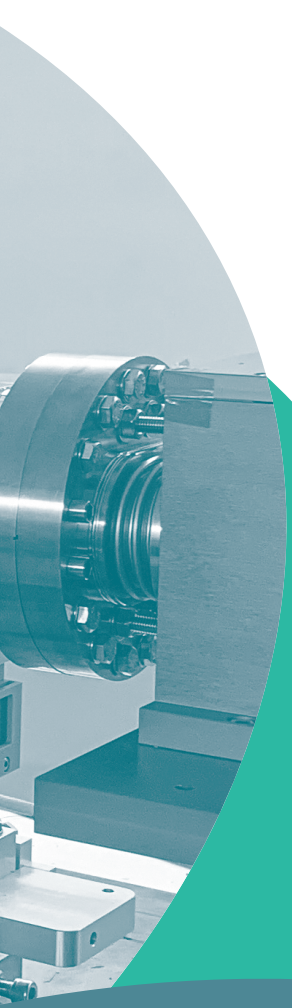

Facility Development and Status

Status of TLS and TPS Accelerators

Taiwan Light Source (TLS)

Machine Parameters of the TLS

The Taiwan Light Source (TLS) celebrated its 30th anniversary of first light in 2023. Having provided light source services for 32 years since it began operation in 1993, TLS has invited experimental proposals and opened its facilities to users, initially featuring three soft X-ray beamlines: HSGM, LSGM, and Seya. The original TLS design was based on a triple bend achromat lattice with a beam energy of 1.3 GeV and a beam current of 200 mA. Following several phases of upgrades, the accelerators now achieve a beam energy of 1.5 GeV, a maximum stored beam current of 360 mA, top-up injection, a superconducting radio-frequency (SRF) cavity, a liquid-helium cryogenic system, superconducting wigglers (SCWs), and advanced feedback systems for orbit and bunch-to-bunch stability. Many of these advancements were pioneering and unique in the low-energy synchrotron community. The key parameters of TLS are presented in **Table 1**.

Table 1: Main parameters of the TLS storage ring.

Beam Energy (GeV)	1.5
Number of Buckets	200
Current (mA)	360
Horizontal Emittance (nm-rad.)	22
Vertical Emittance (pm-rad.)	88
Tunes (ν_x/ν_y)	7.303/4.175
Lifetime (hour)	> 6

The storage ring, designed with sixfold symmetry, features four room-temperature undulators, one wiggler, and five SCWs, giving TLS the most densely packed SCW configuration in the community. SCWs generate high-energy photons to support X-ray users. The specifications of the insertion devices are detailed in **Table 2**.

Table 2: Main parameters of the insertion devices used in TLS.

	W200	U50	U90	EPU56	SWLS	SW60	IASWA	IASWB	IASWC
Type	Hybrid	Hybrid	Hybrid	Pure	SC	SC	SC	SC	SC
Period Length (mm)	200	50	90	56	250	60	61	61	61
Photon Energy (eV)	800–15k	60–1.5k	5–500	80–1.4k	2k–38k	5k–20k	5k–20k	5k–23k	5k–20k

Statistics of TLS Machine Operation

During the initial top-up injection phase, the stored beam current was limited to 200 mA in early 2005 due to constraints of the RF system capabilities and beam stability. Following the installation of the SRF module and the upgrade of the feedback system, TLS gradually increased the stored beam current to 360 mA after 2010. **Figure 1** presents the performance metrics of TLS operations from 2011 to 2025. Availability is defined as the ratio of actual user time to scheduled user time; mean time between failures (MTBF) is defined as the ratio of scheduled user time to the number of system faults; and the beam stability index is evaluated based on photon intensity variation in the diagnostic beamline, maintained within 0.1%.

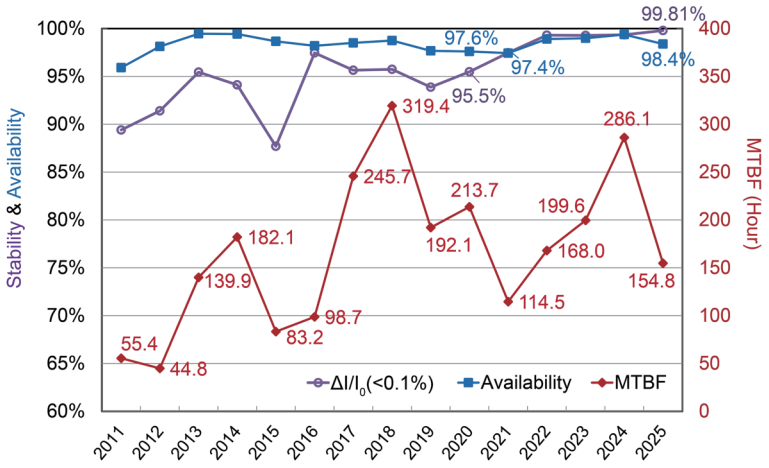

Fig. 1: Annual beam stability index of 0.1%, availability, and MTBF for the TLS.

In 2025, the annual availability of TLS reached 98.4%, with scheduled user time totaling 4,488 hours, an MTBF of 154.76 hours, and beam stability of 99.81%. The primary reason for the low MTBF this year was six abnormal voltage sag events from Taiwan Power Company (TPC), occurring once in March, three times in April, and twice in November. These voltage sags caused damage to high-voltage-sensitive critical subsystems, which triggered multiple beam trips.

Downtime and Failure Analysis of the TLS

In 2025, there were 28 beam trips and a total of 72.02 hours of downtime. The SRF system, which provides high power to the stored beam and operates at 4.5 K, is complex and requires a strict interlock protection system. This system accounted for the largest portion of the annual downtime but has a fast recovery time. **Figures 2 and 3** summarize the contributions of each subsystem to the overall performance of the TLS facility. The primary causes of downtime this year were six force majeure voltage drops, where three events in April were particularly impactful. These voltage drops induced six consecutive trips of the unstable pulser power supplies during injection operations. Additionally, five emergency power feeder phase-loss incidents in late November and December led to four RF system trips and an extended recovery period. These events highlight the need to evaluate the replacement of aging infrastructure and to strengthen power grid stability to ensure reliable operation in the future.

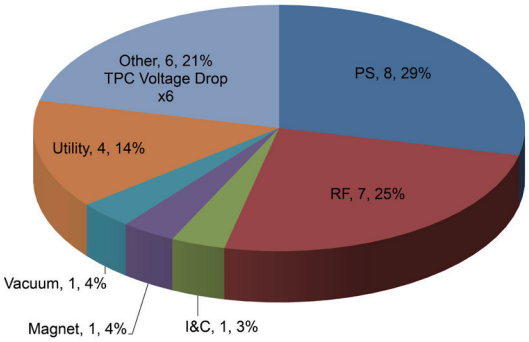

Fig. 2: Proportions of beam trips for the TLS accelerators in 2025 (28 trip events in total). The labels in the pie chart indicate the subsystem, number of events, and percentage, respectively. PS: power system; RF: radio frequency; I&C: instrumentation and control. "Other" includes 6 voltage drops caused by TPC.

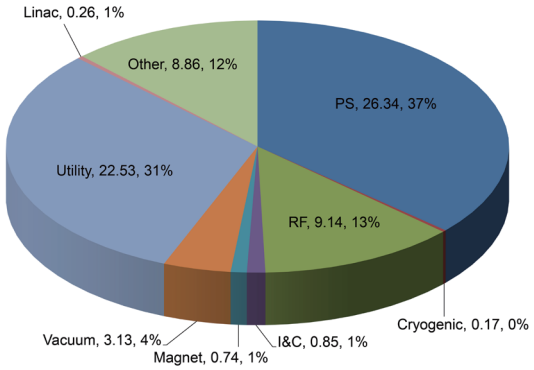

Fig. 3: Downtime distribution for the TLS accelerators in 2025 totaled 72.02 hours. The major sources of failure were: PS, 26.34 hours; Utility, 22.53 hours; RF, 9.14 hours; and Other, 8.86 hours.

Taiwan Photon Source (TPS)

Machine Parameters of the TPS

The TPS has been operational for nine years, having officially opened to user proposals in 2016. The TPS storage ring uses a strong focusing DBA lattice, which provides low emittance, top-up injection, SRF module operation, long straight sections, and high stability. The main parameters of the TPS storage ring for current operation are listed in **Table 3**. The TPS accelerators consist of concentric storage rings and booster rings within the same tunnel, a design chosen due to limited campus space and energy requirements.

Table 3: Main parameters of the TPS storage ring.

Beam Energy (GeV)	3
Circumference (m)	518.4
Current (mA)	500
Number of Buckets	864
Beam Emittance ($\varepsilon_x/\varepsilon_y$) (nm-rad.)	1.6/0.016
Momentum Compaction (α_1/α_2)	0.0024/0.0021
Tunes (ν_x/ν_y)	26.15/14.23
Lifetime (hour)	> 8

Statistics of TPS Machine Operation

The TPS began operations for users in the last quarter of 2016 with a beam current of 300 mA. This was increased to 400 mA in December 2017, and the system continued to operate regularly until it reached 450 mA on the last day of 2020. In 2021, the stored beam current reached 500 mA. To meet the needs of user experiments, we now provide both hybrid mode and uniform filling mode operation at a total current of 500 mA. In hybrid mode, 560 tightly packed electron bunches are placed in the storage ring along with one isolated high-charge single bunch in the remaining gap. This configuration supports both high-current/high-flux multi-bunch experiments and time-resolved measurements using the single bunch (**Fig. 4(a)**, see next page). Conversely, in uniform filling mode, the electrons are evenly distributed around the ring, typically with 800 or more bunches, resulting in a smooth and stable beam current profile that benefits high-current and steady photon-flux applications (**Fig. 4(b)**).

The scheduled and delivered user times, along with availability, are shown in **Fig. 5** on a quarter-to-quarter basis since 2017. For 2025, the scheduled user time is 4,904 hours, of which 1,968 hours will be operated in uniform filling mode. The annual availability of TPS reached 98.7%, with a highest MTBF of 222.9 hours, as shown in **Fig. 6**.

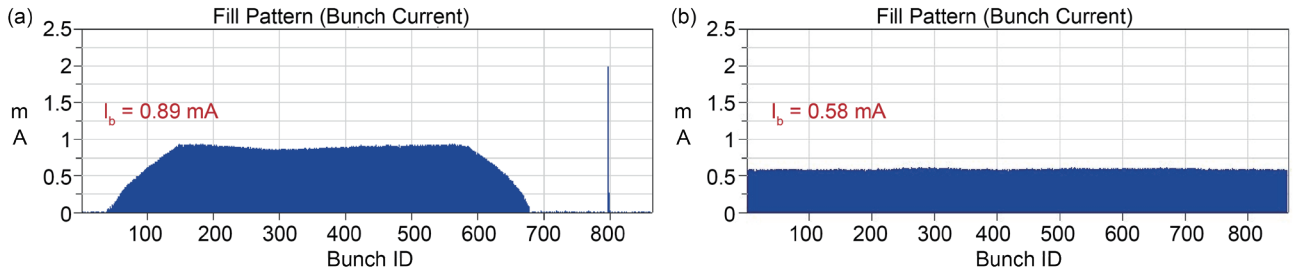

Fig. 4: (a) Hybrid mode and (b) uniform filling mode operation.

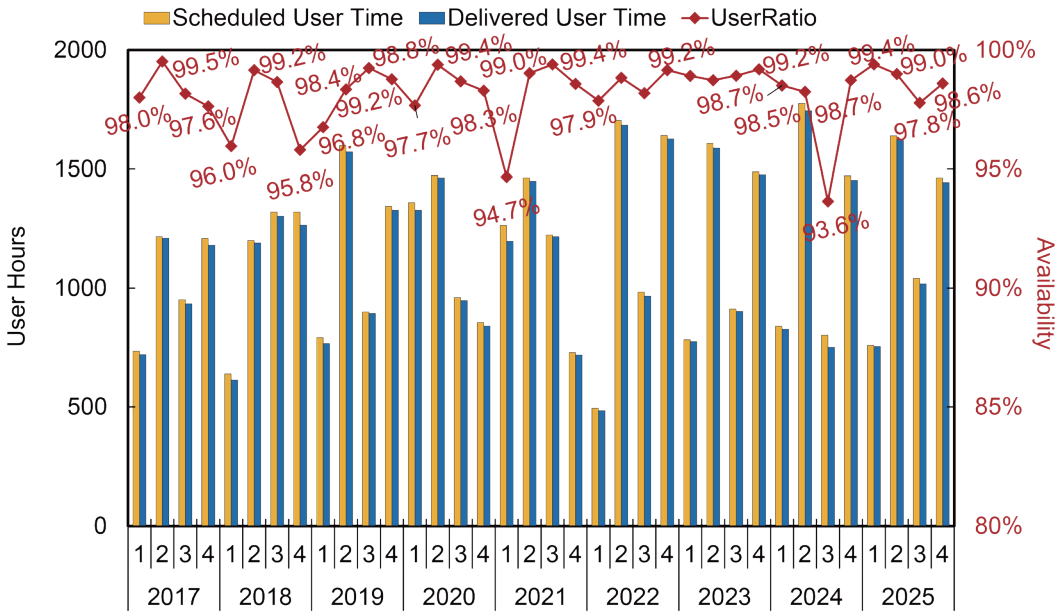

Fig. 5: User time and beam availability at the TPS from 2017 onward.

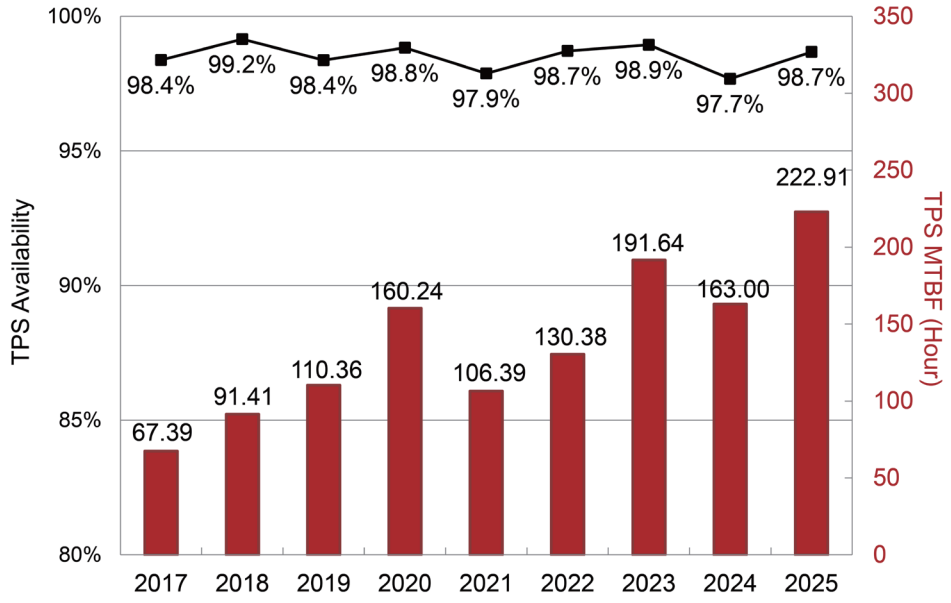

Fig. 6: MTBF and beam availability at TPS from 2017 onward.

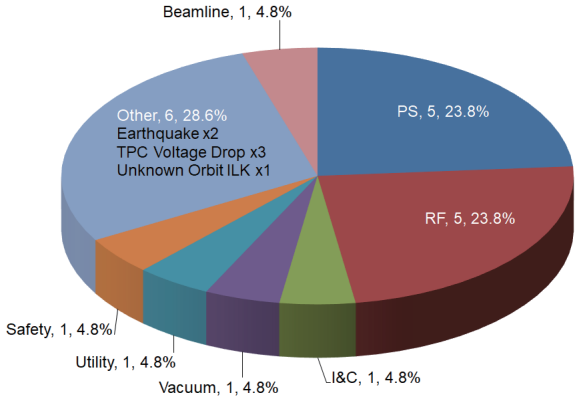

Fig. 7: Ratios of beam trips for the TPS accelerators in 2025 (21 trip events in total).

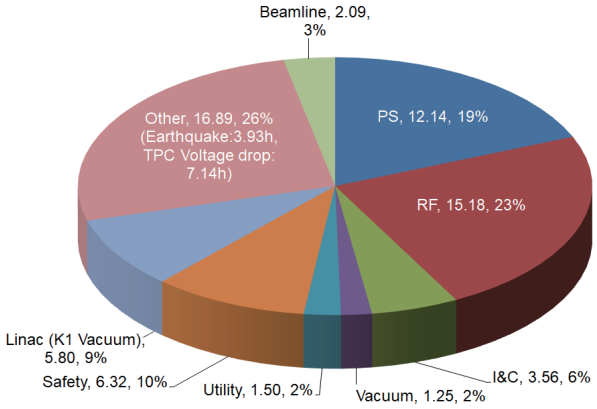

Fig. 8: Proportions of downtime in the TPS accelerators in 2025 (64.73 hours in total). The major downtime contributors are as follows: RF, 15.18 hours; Other, 16.89 hours; PS, 12.14 hours; and Safety, 6.32 hours.

Downtime and Failure Analysis of the TPS

In 2025, there were 21 beam trips and a total of 64.73 hours of downtime. **Figures 7 and 8** illustrate the contributions of each subsystem within the TPS facility to these beam trips and downtime. The PS and SRF subsystems were the most frequently involved in these incidents. The higher failure rate of the SRF system is attributed to sensor aging, solid-state module damage, and cooling system leakage, all resulting from prolonged operation at a high current of 500 mA. Nevertheless, excluding trips caused by earthquakes and unexpected voltage drops by TPC, the overall reliability of these subsystems has significantly improved in recent years, enabling stable operation and extending the MTBF. (Reported by Hung-Jen Tsai)

Feasibility Study for TPS Upgrade: 6BA Solution

The Taiwan Photon Source (TPS) has been in successful user operation since 2016, delivering high-brightness synchrotron radiation source for diverse scientific purposes. Considering that the typical lifecycle of a storage-ring light source is 20–30 years, NSRRC has initiated a feasibility study for upgrading TPS to a next-generation, referred to as TPS-II.

Motivation and Design Concept

TPS is a 3 GeV, 518.4 m storage ring housed in a common shielding tunnel with its booster. It provides synchrotron radiation spanning from soft to hard X-rays, achieving a peak brightness of approximately 10^{21} photons/s-mm^2-mrad^2-0.1%BW at 10 keV. While the primary objective of the upgrade is to enhance scientific capabilities, energy sustainability is also a key motivation. The new lattice aims to reduce beam emittance by at least tenfold compared to TPS, resulting in an order-of-magnitude increase in its brightness and coherence fraction. This would allow for shorter sampling times, higher data throughput, and more efficient experiments.

The study focuses on an upgrade constrained by the existing tunnel. The tangential angle of all beamlines must remain unchanged to preserve the utility of existing experimental hutches. The straight sections must remain longer than 5 m to accommodate current insertion devices and RF modules. This compact design necessitates combined-function magnets, compact beam position monitors, and Non-Evaporable Getter (NEG)-coated vacuum chambers. Permanent magnets are planned for use in the arcs, which would not only create essential space for vacuum and diagnostic components but also significantly reduce power consumption. To maintain operational flexibility, the quadrupoles adjacent to the straight sections and the multipoles along the ring will remain electromagnets. Additionally, to ensure beamline performance, longitudinal-gradient bends— in which the center field is higher— are incorporated at the specified angle. This study follows the successful third- to fourth-generation upgrades, such as ESRF-EBS,[1] APS-U,[2] and SLS 2.0,[3] which adopted the MBA[4] or HMBA[5] concepts.

Toward Ultra-Low Emittance: Strategic Choices and Estimated Performance

To identify the optimal path, the team evaluated various lattice configurations, balancing competing scientific, engineering, and facility constraints. Although minimizing beamline realignment is desirable, maintaining the storage ring circumference is critical to avoid the consequential RF synchronization risks. Additionally, feasible magnet strengths are essential for realistic manufacturing and reliable operation.

Prioritizing long-term competitiveness and machine robustness, the 6BA lattice was selected as the primary candidate. This configuration offers a strategic balance: by releasing the strict constraint on source-point offset, a robust lattice can be achieved while retaining the circumference and using feasible magnet specifications. This approach ensures beam stability and high brightness, in addition to freeing up essential space in the arcs for vacuum and diagnostic systems. **Figure 1** depicts the optical functions of the arc connecting the short and long straight sections. The main parameters of the 6BA candidate are summarized in **Table 1**. The error-free lattice has a dynamic aperture (DA) exceeding 7 mm, which is adequate for off-axis injection. The estimated lifetime reaches 9.6 h when operating at chromaticity (1, 3) and assuming a physical aperture with a radius of ±8 mm in the error-free model.

As beam emittance approaches the diffraction limit, intrateam scattering (IBS) remains a bottleneck. Analytical estimates indicate that for a 3 GeV beam with 1.036 nC per bunch, IBS increases the emittance and energy spread by a factor of two when the natural emittance is suppressed below 100 pm-rad. To mitigate this, a third-harmonic cavity and dedicated coupling control are adopted. Upon lengthening the bunch by a factor of three and maintaining a 10 pm-rad vertical emittance, IBS-induced emittance growth can be constrained to 8–25% for natural emittances between 60 and 110 pm-rad.

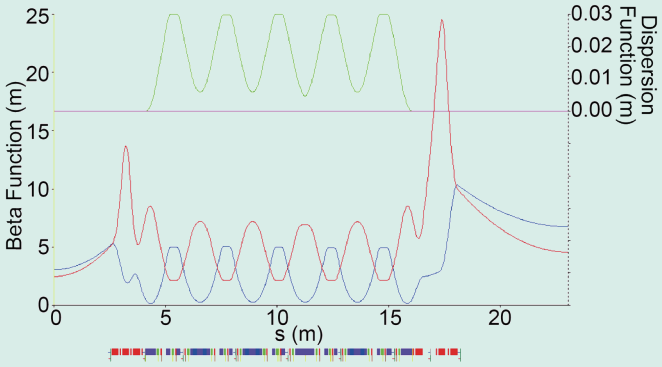

Fig. 1: Optics function of the proposed 6BA lattice. The arrangement of elements is depicted using different colors: blue for dipoles, purple for combined dipoles, red for quadrupoles, and green for sextupoles.

Table 1: Main parameters of TPS and TPS-II.

	TPS	TPS-II 6BA
Emittance (pm-rad)	ε_0 = 1600	ε_0 = 67 → ε_x = 83*
Energy Spread	8.86×10^{-4}	$8.49 \times 10^{-4} \rightarrow 1.01 \times 10^{-3}$*
Tune	(26.15, 13.23)	(66.81,19.74)
Chromaticity	(-75, -29)	(-119, -86)
Momentum compaction Factor	(2.4, 0.21) $\times 10^{-4}$	(0.61, 2.43) $\times 10^{-4}$
Damping Time (ms)	(12.2, 6.1, 6.1)	(12.3, 19.6, 14.0)

* with the inclusion of IBS, κ = 12 %, and a harmonic cavity that stretches the bunch length by a factor of three.

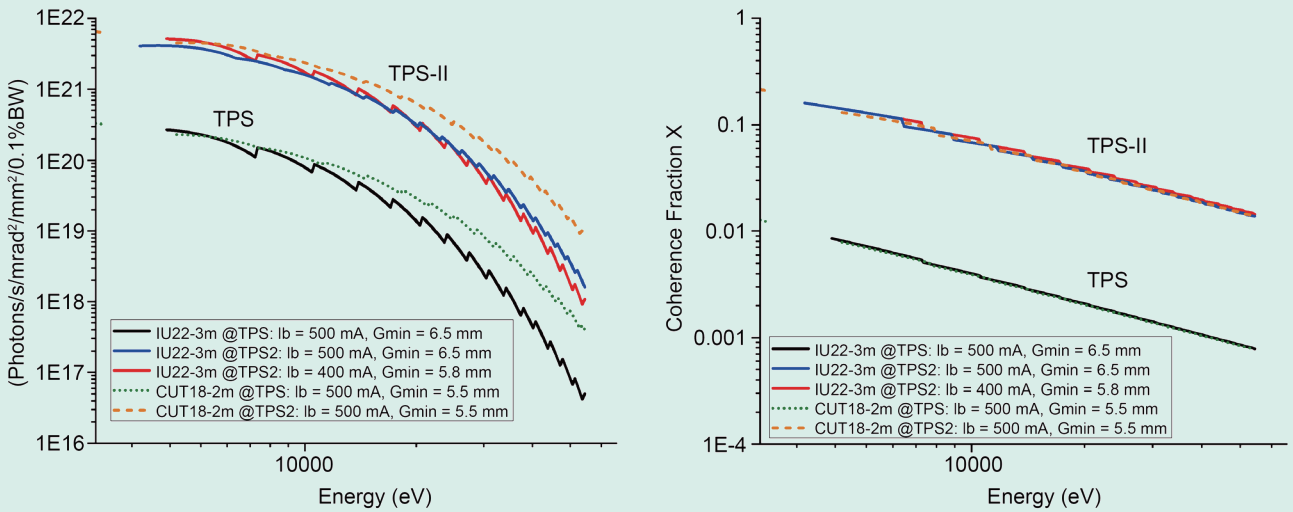

Fig. 2: Estimated performance in brightness and horizontal coherence fraction, assuming a horizontal beam emittance of 94 pm-rad and a coupling coefficient of 10%. [Courtesy of Jui-Che Huang]

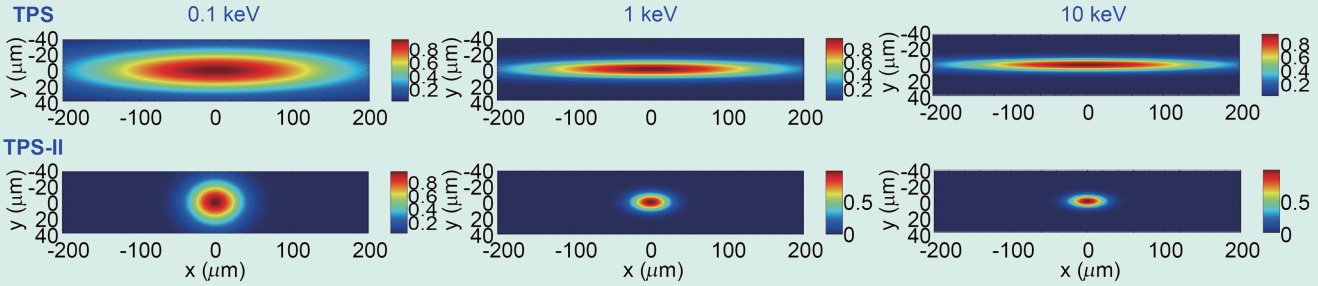

Fig. 3: Photon beam profiles estimated using an undulator at different photon energies for TPS and TPS-II, assuming the same 4 m undulator.

Assuming a horizontal beam emittance of approximately 100 pm-rad, **Fig. 2** shows the estimated brightness and coherence fraction in the hard X-ray region. TPS-II brightness is projected to exceed 10^{21} photons/s/mm^2/mrad^2/0.1%BW, with a corresponding increase in horizontal coherence fraction. **Figure 3** illustrates the estimated photon beam profile from undulator radiation, which evolves from a flat to a nearly round profile, shrinking from approximately 120 to 15 μm (horizontal projection) at 10 keV.

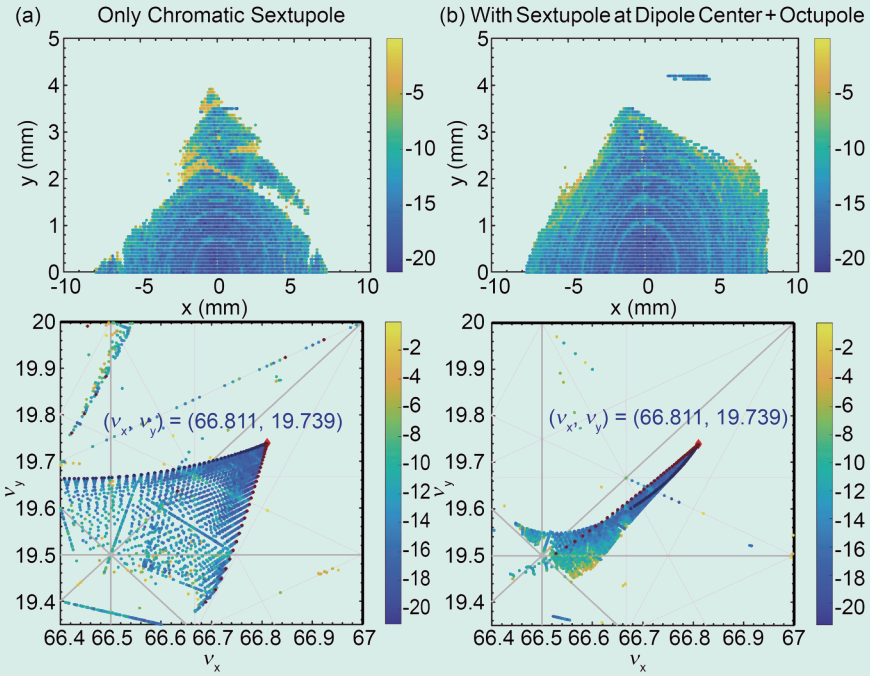

Fig. 4: Tracking the FMA and tune footprint of the 6BA lattice, comparing (a) the baseline configuration and (b) the preliminary proposed configuration.

Lattice Optimization and Dynamics

To construct a robust lattice, a new strategy was developed to control amplitude-dependent tune shift while improving dynamic aperture with minimal degradation of momentum acceptance. This was achieved by allocating weak sextupole components within the dipole center.[6] A unique advantage of this design is the elimination of harmonic multipoles. As a result, the optics near the insertion devices becomes simpler, which allows for independent control of straight sections and improves overall flexibility. Frequency map analysis (FMA) indicated that the dynamic aperture improved significantly from the baseline to the proposed configuration (**Fig. 4**). The density of the tune footprint increased, and the stable region expanded. The feasibility of incorporating sextupole components within the combined dipole is being evaluated, and further nonlinear optimization with realistic machine errors is ongoing.

Supporting Technologies in Development

Parallel to lattice development, several key technologies are actively being developed. These efforts provide the essential foundation for future TPS upgrades.

- Permanent-magnet technology: facilitates the development of stable, energy-efficient magnet systems.[7]
- Nonlinear injection kicker: allows for off-axis top-up injection with minimal disturbance to the stored beam.[8]
- NEG coating: provides distributed pumping for small-aperture vacuum chambers.[9]
- Passive third-harmonic superconducting cavity: supports bunch lengthening, increased lifetime, reduced heat load, and enhanced beam stability.[10]

Outlook and Next Steps

Globally, storage-ring upgrades are trending toward ultra-low emittance and high coherence. As shown in **Fig. 5** (see next page), TPS is well positioned to follow this trend. Future efforts will focus on (1) integrated lattice optimization by incorporating realistic magnet and alignment errors; (2) dedicated coupling control and systematic studies of injection schemes; (3) evaluation of low-alpha lattice impacts and the corresponding countermeasures; and (4) most importantly, continuous engagement with beamline scientists and engineers to refine scientific requirements and technical constraints.

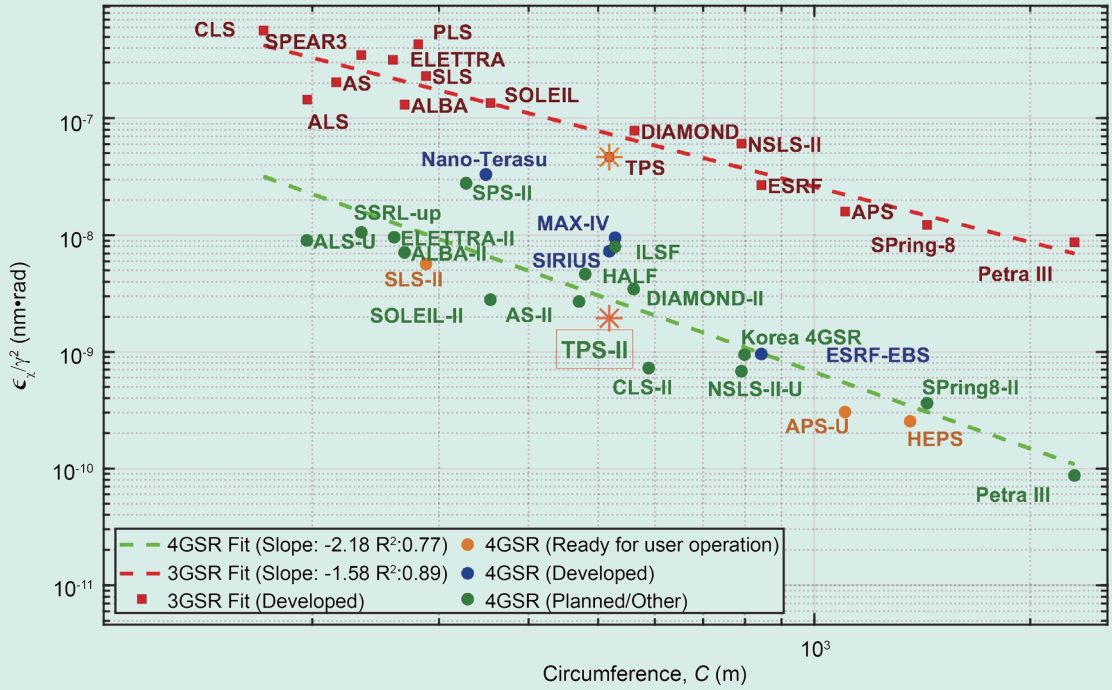

Fig. 5: Statistics of storage rings worldwide showing energy-normalized beam emittance versus circumference. Data compiled from public resources, CDRs, technical reports, and conference proceedings, as of December 2025.

With collaborative efforts throughout the NSRRC, TPS-II can become a next-generation synchrotron source that supports NSRRC's mission to enable cutting-edge research. (Reported by Nuan-Ya Huang)

References

1. P. Raimondi, N. Carmignani, L. R. Carver, J. Chavanne, L. Farvacque, G. Le Bec, S. M. Liuzzo, T. Perron, S. White, Phys. Rev. Accel. Beams **24**, 110701 (2021).
2. V. Sajaev, A. Brill, B. Yang, F. Rafael, G. Shen, H. Bui, H. Shang, J. Dooling, J. Carwardine, J. Calvey, K. Harkay, L. Emery, M. Borland, M. Kelly, N. Arnold, N. Kuklev, O. Mohsen, R. Soliday, R. Lindberg, T. Fors, T. Berenc, U. Wienands, W. Cheng, Y. Sun, Proc. IPAC'**25**, TUCD2 (2025).
3. M. Böge, Proc. IPAC'**25**, WECN1 (2025).
4. D. Einfeld, J. Schaper, M. Plesko, Proc. IPAC'**95**, 177 (1995).
5. ESRF-EBS, EBS Storage Ring Technical Report, September (2018).
6. N.-Y. Huang, F.-H. Tseng, M.-S. Chiu, P. J. Chou, H.-W. Luo, "Toward a Robust TPS-II 6BA Lattice", to be presented at IPAC'**26**, Deauville, France (2026).
7. Y. L. Chu, Y. Y. Hsu, J. C. Jan, H. Chen, C. K. Yang, C. W. Chen, C. S. Yang, J. C. Huang, IPAC'**24**, TUPR51 (2024).
8. C. C. Chang, C. K. Chan, B. Y. Chen, C. S. Huang, C. Y. Yang, F. Y, Lin, C. S. Fang, K. K. Lin, J. H. Kang, Vacuum **239**, 114356 (2025).
9. G.Y. Hsiung, C. Shueh, C.M. Cheng, C.K. Chan, R. Valizadeh, Vacuum **234**, 114112 (2025).
10. C. H. Lo, M. C. Lin, Y. C. Hsu, M. K. Yeh, F. Y. Chang, Z. K. Liu, IEEE Trans. Appl. Supercond. **35**, 5 (2025).

Development of a Nonlinear In-Vacuum Kicker at the TPS

To improve beam injection performance and reduce perturbations of the stored electron beam, the development of a novel nonlinear in-vacuum kicker (NIK) system for the Taiwan Photon Source (TPS) has been initiated. This effort aims to upgrade the injection process by replacing the traditional four-kicker method with an advanced, low-disturbance solution.

At present, TPS uses a conventional four-kicker injection system, which consists of four identical kicker magnets and two septa to guide the injected beam into the storage ring, as illustrated in **Fig. 1(a)**. Although this method is widely adopted, it introduces oscillations and positional shifts in the stored beam, which are especially problematic under the tight dynamic aperture conditions required by next-generation light sources. In response to these limitations, the TPS team is developing a nonlinear injection scheme, as illustrated in **Fig. 1(b)**.[1] This scheme includes a custom-designed NIK that generates a strong, localized magnetic field to bend the incoming beam while maintaining a nearly zero field along the trajectory of the stored beam. A major innovation of this system is its in-vacuum design, which differs from the more common out-of-vacuum setups used in other facilities. During testing, the four-kicker system and the NIK scheme will coexist. In this phase, the NIK will operate while the four-kicker system is switched off. Once the injection efficiency meets the required performance targets and the operational reliability of the NIK is fully demonstrated, the NIK scheme will replace the existing four-kicker configuration in the final implementation.

The NIK provides several unique advantages:

- Compact geometry: the vacuum-integrated configuration allows for a reduced vertical gap between the copper coils, which increases the magnetic field strength available to deflect the injected beam.
- Lower cost and simplified construction: by using multiple ceramic components instead of a monolithic coated ceramic chamber, the system eliminates the need for complex coating processes and reduces costs.

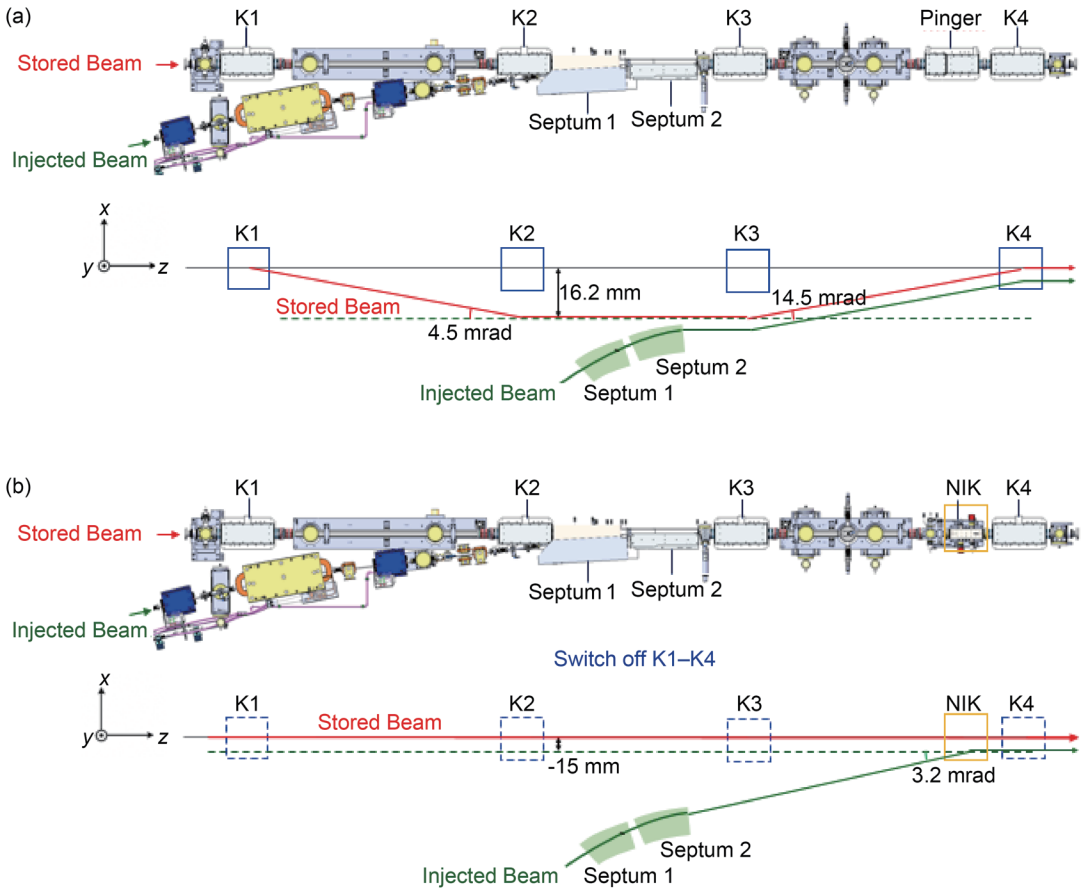

Fig. 1: (a) Existing injection scheme using four bumper kickers, and (b) proposed injection scheme with a NIK kicker in the TPS injection section. [Reproduced from Ref. 1]

- Improved coating uniformity: titanium coatings applied to flat ceramic substrates offer better thickness control while maintaining variation within 5% compared to coatings on the inner walls of cylindrical chambers.
- Lower inductance: the internally routed coil connection reduces the system's total inductance compared to conventional external wiring, thereby increasing efficiency during pulsed operation.

The NIK assembly comprises a titanium vacuum chamber, ceramic substrates, support blocks, and end plates. As shown in **Figs. 2(a) and 2(b)**, the structure contains eight copper coils embedded in grooves on the ceramic substrates, resulting in a significantly more compact design compared to the original kicker shown in **Fig. 2(c)**.[1,2] Precise assembly is achieved using ceramic clamping blocks and titanium screws to ensure accurate coil placement and mechanical robustness under vacuum conditions. The vacuum chamber is made from Grade 2 titanium, which has been selected for its low thermal outgassing, non-magnetic behavior, and light weight. Titanium plates are welded together to form the chamber, including two DN35CF flanges on each side for installing K-type thermocouples, vacuum gauges, and NEXTorr Z 200 vacuum pumps. Additionally, eight DN16CF ports (four on the top and four on the bottom) are provided, with designated ports used as electrical feedthroughs for the kicker coil connections.

To ensure adequate electrical conductivity for the passage of beam image currents, a titanium coating is applied to the ceramic substrates. Increasing the coating thickness can reduce ohmic heating and thermal stress, but it also increases eddy current losses, which raises power deposition, attenuates the magnetic field, and slows the temporal response of the pulsed field. Therefore, achieving an optimal balance is critical. The selected coating thickness of 5 μm provides sufficient electrical conductivity while minimizing heating from both image and eddy currents, thereby ensuring stable magnetic field performance and effective thermal management.

The core design of the NIK generates a nonlinear pulsed magnetic field that peaks at the injected beam position while maintaining a flat zero-field region around the stored beam. This field-free zone spans ±1.5 mm centered on the stored beam trajectory. The nominal peak field is 890 G at an offset of 15 mm. However, the nonlinear characteristics of conventional magnetic yoke materials can induce unwanted residual fields near the center. To avoid these fields, the NIK is designed without a yoke. Consequently, a high current is required to generate the necessary field strength. Therefore, the entire NIK is implemented as an in-vacuum type structure, which allows the magnet gap to be minimized, thereby improving magnetic efficiency and field control.

Magnetic field simulation studies highlight the impact of return conductor configuration. A symmetric return path, as shown in **Fig. 3(a)**, produces opposing vertical fields in the upper and lower conductors, which effectively cancel each other and expand the field-free region at the beam axis. By contrast, an asymmetric design, as shown in **Fig. 3(b)**, leaves residual magnetic fields that may introduce undesirable quadrupole components. Positioning errors in conductor placement further compromise field uniformity, as shown in **Fig. 3(c)**.[3]

An in-house measurement system was developed to verify the field characteristics of the NIK, as shown in **Fig. 4**.[3] The setup included a function generator (DG 535), digital oscilloscope (TDS3054B), current transformer, and long coil probe with an RC integrator circuit. The long coil probe was constructed using printed circuit board (PCB) technology to ensure precise conductor positioning. This system was used to capture the dynamic magnetic response of the kicker during pulsed operation.

Figure 5 presents a comparison between the simulated and measured profiles of the kicker's first magnetic field integral. At the center of the beam trajectory, the ideal value is zero, and the measured deviation is approximately 250 G·cm. At the design injection point (-15 mm), the simulated and measured values of the field integral are approximately -32,100 G·cm, with a relative error of just 0.124%, which is well within the expected tolerance range.[3]

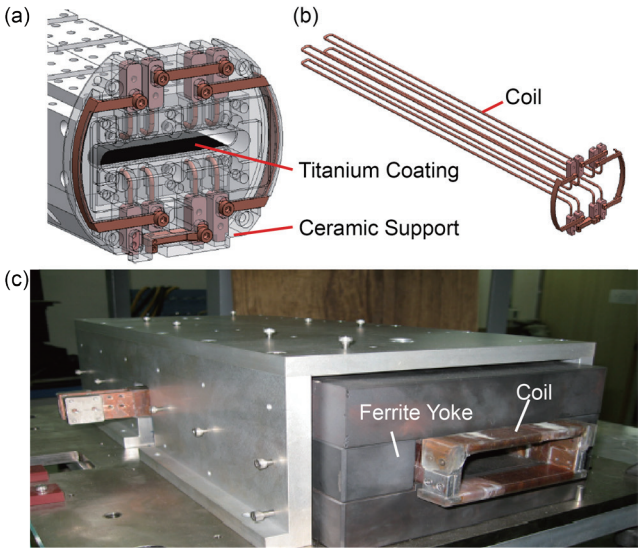

Fig. 2: Routing of copper coils (a) with and (b) without the surrounding ceramic support structure, and (c) one of the four-kickers. [Reproduced from Refs. 1 and 2]

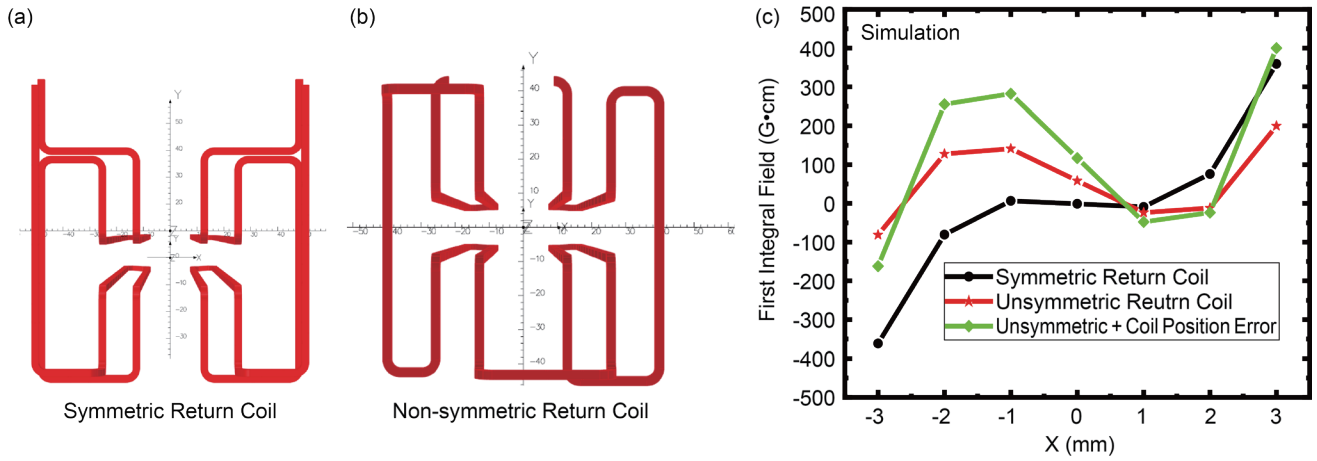

Fig. 3: Symmetric and non-symmetric coil designs. [Reproduced from Ref. 3]

To evaluate the vacuum compatibility of the NIK system, which is composed of ceramics, titanium, copper, stainless steel, aluminum alloy, and Kapton, we measured its outgassing rate using the pressure-rise and throughput methods. A dedicated test bench was built, and the NIK was connected to an aluminum orifice chamber *via* a gate valve and pumped using a turbo molecular pump. Two ion gauges were used to monitor pressure changes in both chambers. After 120 h of pumping, the pressure dropped below 5×10^{-7} mbar, indicating good initial vacuum performance. Subsequently, a bake-out at 150 °C for 24 h was conducted to further reduce gas release. The measured thermal outgassing rate was 1.9×10^{-8} mbar·L/s, consistent across both measurement methods. After the bake-out, two NEXTorr Z200 pumps were installed and activated. The final pressure reached the 10^{-10} mbar range, confirming the system's suitability for ultrahigh vacuum applications.

To minimize interference with user experiments during injection, the NSRRC is committed to developing a transparent injection approach using this nonlinear in-vacuum kicker. A key achievement is the system's low inductance value of 1.56 μH, which allows for faster current rise times and improved pulse shaping.

This development represents a major step forward for TPS and contributes to the long-term goal of upgrading the injection system for TPS-II, the next-generation storage ring. With its improved field characteristics, reduced beam disturbance, and robust vacuum performance, the nonlinear kicker will support future high-brightness and low-emittance beam operations. (Reported by Chin-Kang Yang and Chin-Chun Chang)

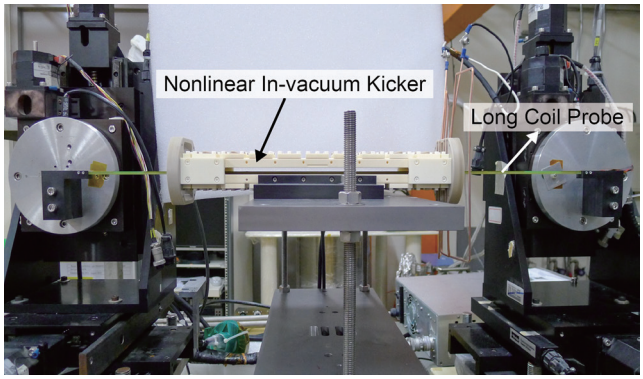

Fig. 4: NIK field measurement setup. [Reproduced from Ref. 3]

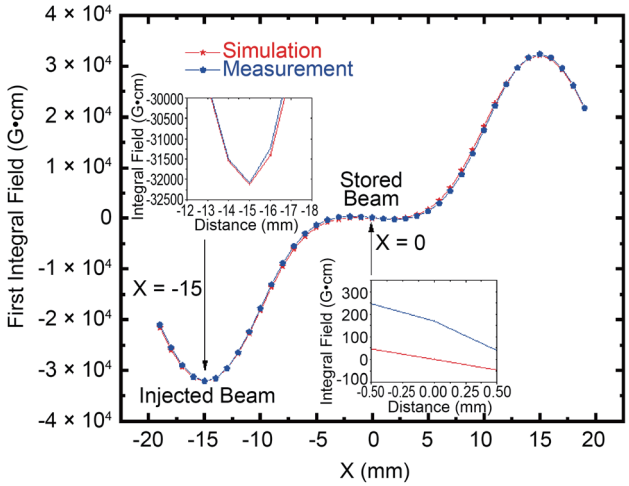

Fig. 5: Simulated and measured first magnetic field integral profiles. [Reproduced from Ref. 3]

References

1. C.-C. Chang, C.-K. Chan, B.-Y. Chen, C.-S. Huang, C.-K. Yang, F.-Y. Lin, C.-S. Fang, K.-K. Lin, J.-H. Kang, Vacuum **239**, 114356 (2025).
2. C. H. Chang, C. S. Yang, P. J. Chou, P. Chang, C. K. Chan, C. S. Fann, Y. H. Liu, J. C. Huang, C. S. Hwang, J. R. Chen, Proc. PAC'**09**, 190 (2009).
3. C.-K. Yang, F.-Y. Lin, H. Chen, H.-H. Chen, Y.-L. Chu, Proc. IPAC'**24**, 3264 (2024).

TPS LINAC Pulsed High-Power RF System Upgrade

The pre-injector of the Taiwan Photon Source (TPS) is a linear accelerator (LINAC)-based system consisting of five major components:

1. Direct current (DC) thermionic electron gun: supports single-bunch mode (SBM, pulse width 1 ns, output charge 2 nC) and multi-bunch mode (MBM, pulse width 200–1000 ns, output charge 5 nC). The maximum repetition rate for both modes is 5 Hz. After acceleration in the electron gun, the beam energy reaches 90 keV.
2. Sub-harmonic pre-buncher: a single-cavity resonator operating at 499.654 MHz that compresses the electron beam pulse width to below 1 ns.
3. Primary buncher: consists of four resonant cavities operating in the 2π/3 mode at 2997.912 MHz (40 °C). It accelerates the electron beam from 90 keV to 300 keV and requires 2 MW of radio-frequency (RF) input power.
4. Final buncher: consists of 16 resonant cavities operating in the 8π/9 mode at 2997.912 MHz (40 °C). It further accelerates the beam from 300 keV to 3 MeV and requires 3.5 MW of RF input power.
5. S-band linear accelerator: includes 156-cell traveling-wave structure operating in the 2π/3 mode at 2997.912 ± 0.03 MHz and maintained at 38–42 ± 0.1 °C. This final stage consists of three S-band accelerator sections (LINAC-ACC1 to ACC3), which raise the beam energy to 150 MeV. Each section requires roughly 16 MW of RF power. **Figure 1** shows the TPS injector system,[1] which was designed and manufactured as a turnkey system by Research Instruments (RI).

Klystron Upgrade

The TPS injector system is powered by three pulsed high-power RF stations. The first RF station (K1) supplies RF power to the Primary Buncher, Final Buncher, and LINAC-ACC1, while the second (K2) and third (K3) stations supply RF power to LINAC-ACC2 and LINAC-ACC3, respectively.

All three stations currently use the Thales TH2100A Klystron (**Fig. 2(a)**).[2] The electron gun in this Klystron has long been associated with a relatively high arcing rate, which is a common cause of failure. Additionally, declining manufacturing quality in recent years has shortened operational lifetimes, directly affecting the reliability of TPS operations.

To address these issues, a Klystron Upgrade Program was initiated in 2024 to replace the TH2100A with the E37310A Klystron (**Fig. 2(b)**)[3] manufactured by Canon Electron Tubes & Devices (CETD). As summarized in **Table 1**, the E37310A's performance and operating parameters are similar to those of the TH2100A and meet TPS LINAC requirements. Experience from the Taiwan Light Source (TLS) LINAC upgrade shows that the E37310A provides

Table 1: Comparison of the specifications of the Thales TH2100 and CETD E37310A Klystrons.

	Thales TH2100	Canon E37310A
Frequency (MHz)	2998.5 ± 1	2998.5 ± 1
Peak Cathode Voltage (kV)	272	295
Peak Cathode Current (A)	286.2	310
Drive Power (W)	126.7	291
Peak RF Output Power (MW)	35.1	35.6
Pulse Width (duration, 75%) (μs)	6.5	7.5
Pulse Width (duration, RF) (μs)	4.5	4.5
Pulse Transformer Turn Ratio	13	14
Klystron Impedance (Ω)	5.62	4.7

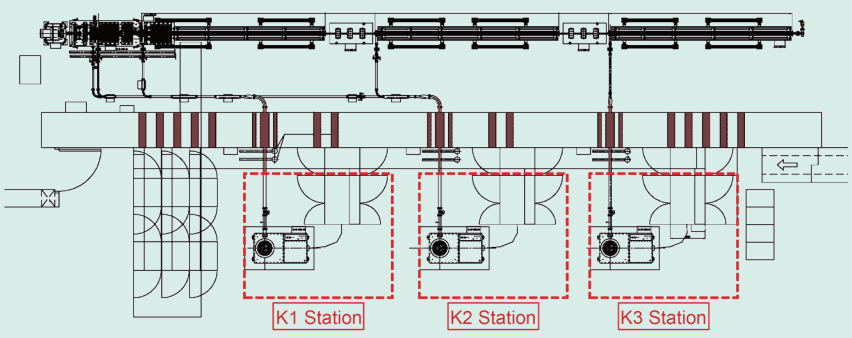

Fig. 1: TPS injector system. [Reproduced from Ref. 1]

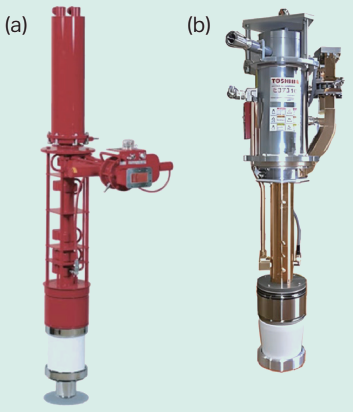

Fig. 2: (a) Thales TH2100 Klystron [Reproduced from Ref. 2] and (b) CETD E37310A Klystron [Reproduced from Ref. 3].

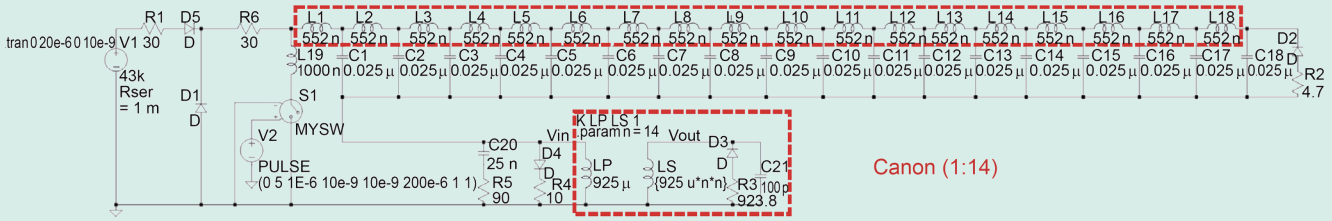

Fig. 3: Circuit model of the newly designed PFN in the pulsed modulator.

excellent operational stability and enhances overall light-source performance. The upgrade also requires modifications to the high-voltage insulating oil tank and the pulsed modulator system to ensure reliable long-term operation.

Klystron Modulator Upgrade

The RI-designed pulsed modulator uses a charging power supply with a maximum output voltage of 45 kV, the upper safety limit for air operation. Under matched conditions, the maximum deliverable primary-side voltage is 22.5 kV. Because different Klystrons require different operating voltages, the transformer turn ratio must be selected carefully, which affects the Klystron oil-tank design.

The Pulse Forming Network (PFN) consists of 18 sections, each with an inductance of 800 nH and a capacitance of 25 nF, resulting in a calculated PFN impedance of 5.66 Ω (design range: 5–6 Ω). The TH2100A operates at 272 kV and 286.2 A, corresponding to a secondary impedance of 950 Ω. With a 1:13 transformer, the primary impedance is 5.62 Ω.

The E37310A operates at 291 kV and 315 A, corresponding to a secondary impedance of 923.8 Ω. With the same 1:13 transformer, the primary impedance becomes 5.47 Ω; however, reaching the required cathode voltage would require 44.77 kV—too close to the system's maximum rating. A 1:14 transformer reduces the primary impedance to 4.7 Ω and requires only 41.57 kV, which remains within specifications. Considering equipment limits, stray inductances, and practical matching constraints, the 1:14 configuration is selected.

The next step is to carry out PFN redesign and optimization. To meet the operating requirements of the E37310A and obtain a flat, sufficiently wide voltage pulse, PFN simulations and design optimization are performed using LT-Spice (**Fig. 3**). Since the PFN capacitances cannot be easily changed, the inductances are redesigned and reduced from 800 nH to 552 nH to achieve the required impedance.

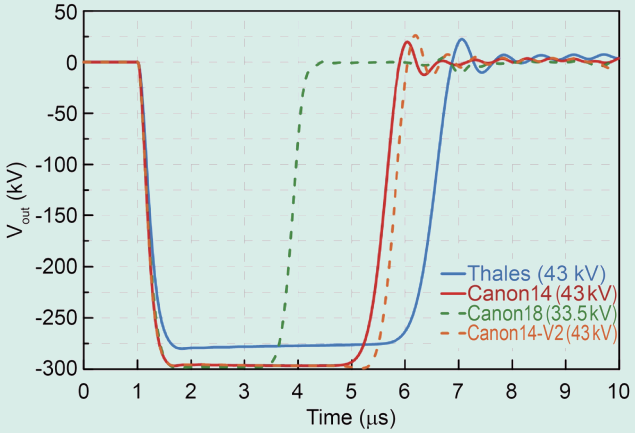

Fig. 4: Circuit-model simulation of the PFN voltage waveforms for the pulsed modulator. Blue: original Thales waveform. Red: Canon PFN with a 1:14 transformer turn ratio. Orange: Canon 1:14 configuration with doubled capacitance in the 18th PFN section. Green: Canon PFN with a 1:18 transformer turn ratio.

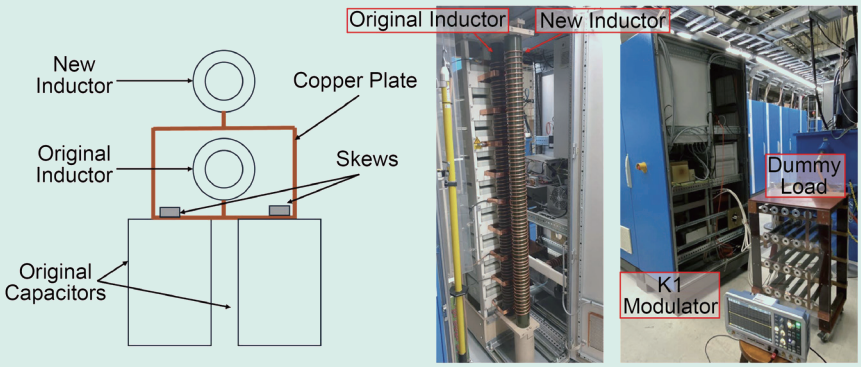

Fig. 5: PFN pulsed modulator: revised configuration diagram and photograph of the completed installation.

Simulation results (**Fig. 4**) show that all turn-ratio configurations produce peak inverse voltages within Klystron specifications. Increasing the transformer ratio from 1:13 to 1:14 shortens the output pulse width by ~1 µs, but overall performance remains acceptable. For comparison, the 1:18 transformer used in TLS reduces pulse width by 2.5 µs, which is unsuitable for TPS.

Doubling the capacitance of the 18th PFN section increases the pulse width by approximately 0.3 µs (**Fig. 4**). A new inductor string is installed in parallel with the original inductors to achieve the required 552 nH. The final PFN configuration and installation are shown in **Fig. 5**.

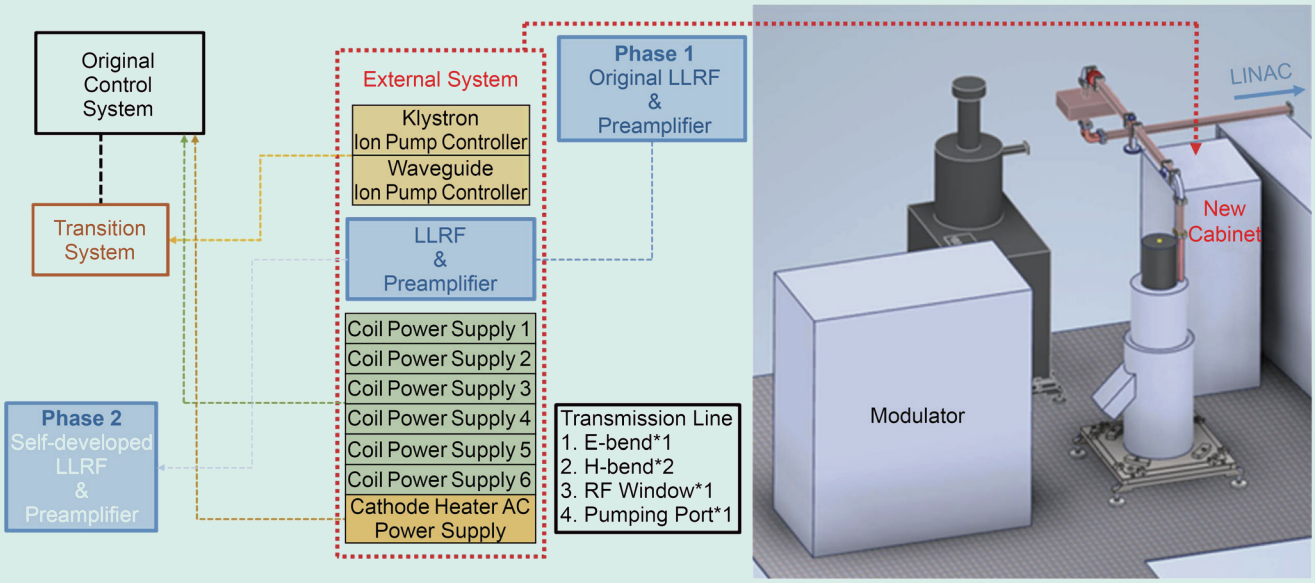

Fig. 6: Revised K1 Station configuration.

Operation Experience with the New Klystron and Modulator

Phase I of the TPS LINAC Klystron upgrade was completed in October 2025. The K1 Station Klystron was replaced with an E37310A, and the pulsed modulator was upgraded. **Figure 6** shows the new system configuration, and **Fig. 7** provides photographs of the installation.

Fig. 7: Installed K1 Station (left) and RF transmission line (right).

Under the test conditions—a pulse repetition rate of 3 Hz, RF pulse width of 4.5 μs, Klystron cathode voltage of 281 kV, and cathode current of 305 A—the E37310A produced 36 MW of RF output power (**Fig. 8**), confirming correct impedance matching and stable modulator performance.

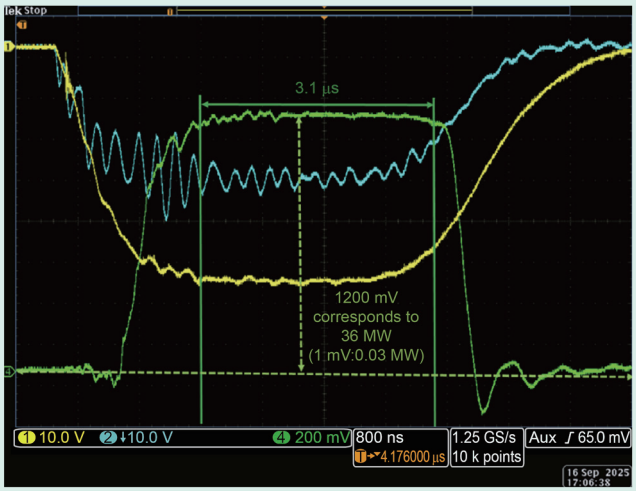

Fig. 8: E37310A Klystron cathode voltage (yellow), cathode current (blue), and RF output power (green).

Conclusion

The redesigned pulsed modulator system achieves a 3.1 μs voltage flat-top, closely matching simulation results and meeting TPS operational requirements. This upgrade also strengthens NSRRC's in-house capability for pulsed modulator development and enhances the potential for future system development.

Extensive testing of TH2100A and E37310A has established standardized operating and maintenance procedures, enhancing safety, efficiency, and reliability. The upgraded RF system has been in routine operation for two months with stable performance.

Phase II of the upgrade will begin in January 2026 and will focus on the K2 Station, further enhancing the stability and reliability of the TPS LINAC. (Reported by Wei-Yuan Chiang)

References

1. TPS 150 MeV Linac Documentation (2008).
2. A. Beunas, THALES RF Sources for Accelerator Recent Developments, July 1 (2019). https://indico.cern.ch/event/804400/contributions/3485023/attachments/1873472/3084546/THALES_presentation_CompactLight_Midterm__Helsinki_2019-rev2-16-9.pdf
3. Microwave Tubes Product Catalog, April (2025). https://etd.canon/en/download/files/microwave_tube_catalog_EN.pdf

Application of AI Intelligent Control in Utility Systems

At the Taiwan Photon Source (TPS), ongoing research is exploring artificial intelligence (AI)-driven methods to enhance energy efficiency across utility systems. Cooling systems account for nearly half of the facility's total energy consumption, making their proper operation essential for reducing overall power demand, as shown in **Fig. 1**. The use of AI for optimizing utility systems is rapidly expanding, particularly in large facilities where chilled water systems and cooling towers represent a significant portion of energy use. AI-based control strategies offer predictive, adaptive, and real-time optimization, providing distinct advantages over traditional rule-based approaches. Studies have demonstrated that AI-driven control can substantially improve both energy efficiency and system reliability in central cooling applications.[1] In critical environments, such as hospitals, advanced optimization methods have achieved considerable energy savings by dynamically adjusting operating parameters in response to changing load and ambient conditions.[2] In complex systems with heterogeneous parallel chillers, neural network-based frameworks have coordinated chiller and cooling tower operations to minimize overall energy use.[3] Building on these advancements, this study applies an AI-based analytical framework to the utility systems at TPS.[4] The model evaluates the impact of ambient wet bulb temperature on overall system behavior and identifies optimal control actions such as adjusting temperature setpoints, pump flow rates, equipment scheduling, and frequency control that can reduce energy consumption while maintaining stable operation. By integrating data-driven modeling with actual operating records, the analysis quantifies potential energy savings and demonstrates that AI-optimized strategies can enhance both efficiency and operational reliability under real-world conditions.

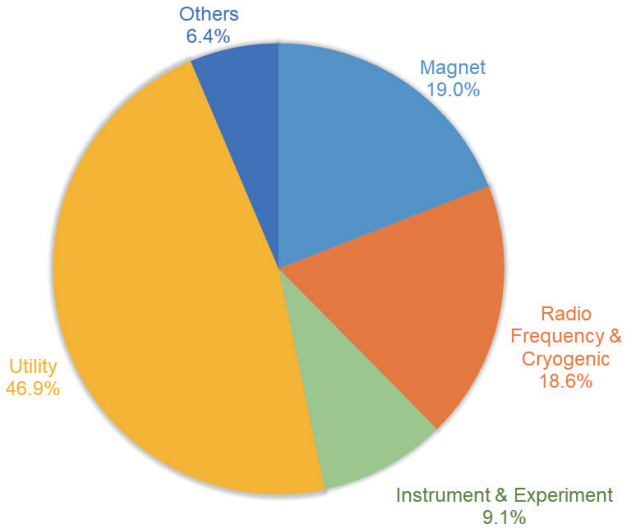

Fig. 1: Power consumption distribution among TPS subsystems.

Model Creation of Cooling Towers and Chilled Water Systems

To improve the efficiency of large-scale cooling and chilled water systems, a data-driven modeling framework was developed. Real-time monitoring was applied to all major equipment, including chilled water pumps, cooling water pumps, chillers, and cooling towers, to collect high-resolution operational data. Each unit operated with independent parameters, enabling flexible and optimal control under varying loads. Power sensors were regularly inspected and calibrated to ensure data accuracy and reliability. System efficiency was assessed by analyzing different operating settings across diverse environmental and load conditions. Machine learning techniques were used to capture nonlinear relationships between equipment behavior and external factors, such as weather and seasonal variations, supporting energy forecasting and early fault detection. Iterative testing and hyperparameter tuning further improved model robustness and predictive accuracy.

Among modeling approaches, recurrent neural networks (RNNs) were selected for their ability to process sequential sensor data, as they retain temporal context unavailable to feedforward networks. To improve long-term dependency learning, the

long short-term memory (LSTM) architecture was adopted. Its memory cells and gating mechanisms mitigate vanishing gradient issues and enhance training stability. The LSTM model demonstrated high accuracy in forecasting energy demand, enabling precise prediction of future power consumption based on historical data. Incorporating external features, such as weather conditions and diurnal patterns, further improved forecast reliability, supporting optimized resource allocation and adaptive control strategies.

To identify the primary factors influencing system energy consumption, we selected eight key input variables based on domain knowledge and sensor availability. These variables include chilled water inlet temperature (T_{in_cw}), chilled water outlet temperature (T_{out_cw}), chilled water flow rate (Q_{cw}), ambient wet bulb temperature (T_{wb}), cooling water temperature setpoint($T_{set\_cooling}$), cooling water inlet temperature ($T_{in\_cooling}$), cooling water outlet temperature ($T_{out\_cooling}$), and cooling water flow rate ($Q_{cooling}$). To enable precise characterization of energy distribution across the system, the output layer was designed to model the power consumption of four major equipment groups separately: chillers ($P_{chillers}$), cooling towers ($P_{cooling\_towers}$), chilled water pumps ($P_{chilled\_water\_pump}$), and cooling water pumps ($P_{cooling\_water\_pump}$). As shown in **Fig. 2**, these output variables represent the total power usage of each subsystem. For consistency, measurement units were standardized as follows: temperature in degrees Celsius (°C), power in refrigeration tons, and flow rate in gallons per minute (GPM). These eight input features and four output variables served as the main training variables for the RNN-based predictive model. To ensure robustness, the system was tested under various operating conditions, including changes in water flow rates, chilled water setpoints, and cooling tower approach values. High-resolution sensors captured system dynamics, yielding 864,000 raw samples. After noise removal and data cleaning, the dataset was aggregated into 28,800 high-quality samples for training, validation, and benchmarking, providing a solid foundation for data-driven energy optimization. Ultimately, this workflow produced a robust surrogate model that accurately characterizes the system's energy performance across different operating conditions.

Hybrid LSTM-Bayesian Optimization of Power Consumption

To enhance optimization capabilities, the LSTM predictive model was integrated into a Bayesian optimization framework. This approach enables systematic exploration of operational parameters to minimize energy use while ensuring system reliability and thermal comfort. Bayesian optimization is well-suited for optimizing expensive black-box functions by using a probabilistic surrogate model to guide the search toward promising regions. Traditional Gaussian process regression (GPR) provides useful uncertainty estimates but scales poorly with large datasets due to its O (n^3) complexity, making it less suitable for high-resolution time-series data. By contrast, LSTM models train efficiently with graphic processing unit (GPU) acceleration and can handle large sequential datasets. Replacing GPR with an LSTM-based surrogate improves both accuracy and scalability while preserving the sample efficiency of Bayesian optimization. This hybrid LSTM-Bayesian optimization framework enables simulation across a wide range of operating conditions and offers robust data-driven guidance for energy performance optimization. As shown in **Fig. 3**, the search input space, defined by practical ranges of temperatures, flow rates, and setpoints, allows the system to identify optimal operating conditions automatically through iterative, intelligent sampling.

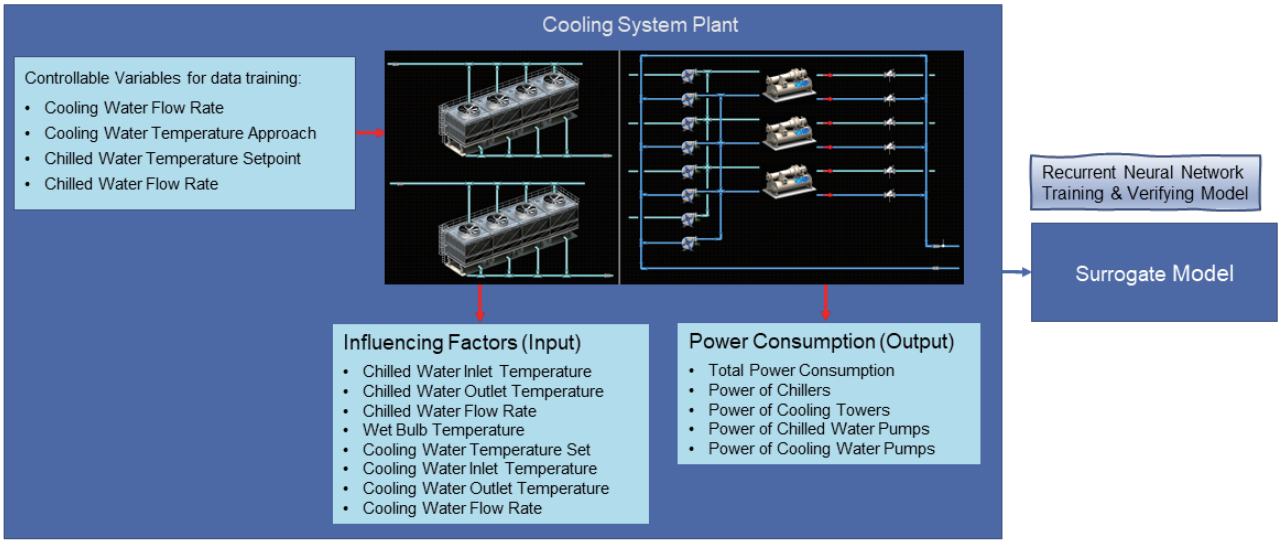

Fig. 2: Schematic diagram of the training model for the cooling tower and chilled water systems. [Reproduced from Ref. 4]

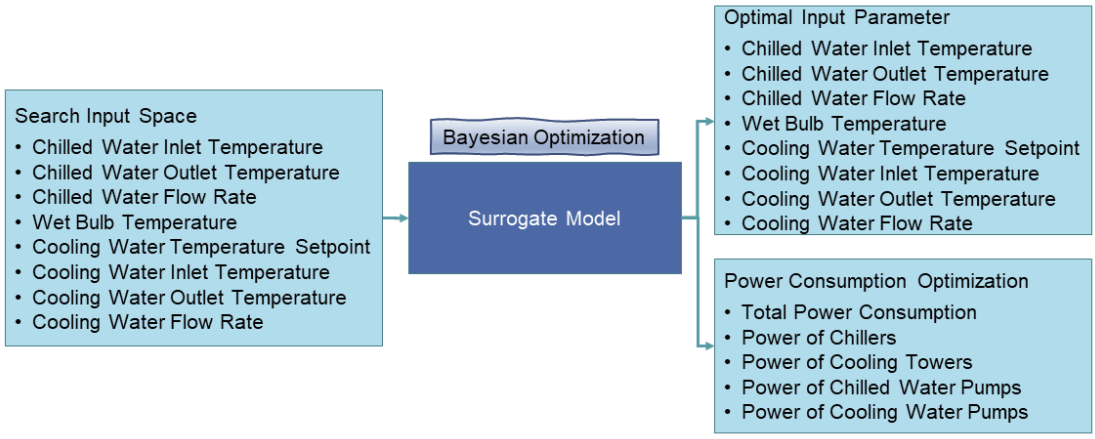

Fig. 3: Schematic diagram of the surrogate model used in Bayesian optimization. [Reproduced from Ref. 4]

Verification of Real-World Operational Adjustments

To validate the predictive model and assess real-world operational impacts, a series of parametric analyses were conducted, focusing on key environmental and control parameters within the cooling system.

Effect of Wet Bulb Temperature on System Power Consumption

The wet bulb temperature represents the thermodynamic lower limit for the outlet temperature of evaporative cooling towers. Regardless of how much cooling capacity is available, the outlet temperature cannot drop below the ambient wet bulb temperature. For efficient operation, the outlet temperature is therefore controlled at the wet bulb temperature plus a fixed 2 °C approach. With the cooling water inlet temperature fixed at 32 °C, the simulation results in **Table 1** show that decreasing wet bulb temperatures reduces chiller power consumption.

By contrast, when cooling tower power rises, pump power remains unchanged due to constant flow rates. As a result, total system power decreases with wet bulb temperature decreases, highlighting the chiller's dominant impact on overall energy use.

Table 1: Effect of wet bulb temperature variation on power consumption.

$T_{set\_cooling}$	T_{wb}	$P_{chillers}$	$P_{cooling\ towers}$	P_{total}
30.0	28.1	1098	99	1398
29.0	27.1	1082	105	1392
28.1	26.1	1060	123	1388
27.0	25.1	1041	132	1377
26.0	24.1	1034	136	1371

Impact of the Cooling Tower Approach on Energy Performance

Although ambient wet bulb temperature cannot be controlled, the approach temperature, defined as the difference between the cooling tower outlet setpoint and the wet bulb temperature, can be adjusted through design and operation. With the cooling water inlet temperature fixed at 32 °C, **Table 2** (see next page) shows that decreasing the approach reduces chiller power consumption while increasing cooling tower power, with the total system energy use still dominated by the chiller. Thus, minimizing the approach temperature is an effective design strategy for improving energy efficiency. This modeling indicates that reducing the approach from 4.0 to 2.0 °C can yield about 1.5% of energy savings. This result supports ongoing hardware upgrades aimed at improving heat-rejection capacity and enabling smaller approach values for better overall system performance. If extrapolation remains valid, an approach of approximately 1.5 °C could potentially deliver up to 1.93% of energy savings.

Table 2: Effect of variations in the cooling tower approach on power consumption.

$T_{set\_cooling}$-T_{wb}	$T_{out\_cooling}$	$P_{chillers}$	$P_{cooling\ towers}$	P_{total}	Efficiency
4.0	29.1	1094	99	1394	0
3.5	28.5	1081	102	1391	0.22%
3.0	28.0	1066	121	1387	0.50%
2.5	27.6	1053	130	1383	0.79%
2.0	27.1	1041	132	1373	1.50%
1.5	26.6	1030	136	1367	1.93%

Influence of Cooling Water Flow Rate

The cooling water flow rate was reduced from 9000 GPM to 6500 GPM, remaining within the safe range required to avoid triggering chiller protection. As shown in **Table 3**, lowering the flow rate significantly reduces cooling water pump power, while chiller and cooling tower power remain largely unchanged. This results in a total energy reduction of 2.78%. Therefore, operating at the minimum flow rate that still meets the chiller's base-load requirements is an effective strategy for improving system efficiency.

Table 3: Effect of variations in the cooling tower flow rate on power consumption.

$T_{cooling\ flow}$	$P_{cooling\ pumps}$	$P_{chillers}$	$P_{cooling\ towers}$	P_{total}	Efficiency
9000	155	1252	129	1585	0
8500	141	1254	127	1575	0.63%
8000	134	1256	130	1572	0.82%
7500	130	1253	135	1567	1.14%
7000	126	1247	138	1558	1.70%
6500	121	1238	134	1541	2.78%

Several practical power-saving measures were evaluated to quantify their potential impact on overall system efficiency. As summarized in **Table 4**, reducing the cooling tower approach temperature yields energy savings of 1.5–1.93%, while lowering the cooling water flow rate provides a 2.78% reduction in total power consumption. Further improvements can be achieved through system-level enhancements, such as using return chilled water to cool deionized water loops (approximately 1.6% of efficiency gain), and installing pressure-independent control valves, which contribute additional savings from both chillers and chilled water pumps. Here, η represents energy efficiency. Adjusting the chiller setpoint also offers substantial energy-saving potential. Depending on the operational scenario, total efficiency improvements can exceed 5.88%, with further gains possible when combined with optimized pump operation, flow control, and temperature management. Collectively, these measures provide a comprehensive pathway for improving system-wide energy performance and support future optimization efforts. (Reported by Zong-Da Tsai)

Table 4: Quantitative evaluation of AI-driven power-saving effects.

Power-saving Measures	Efficiency (%)
Approach Variation	1.5–1.93
Cooling Water Flow Variation	2.78
Deionized Water Cooled with Return Chilled Water (600 GPM)	$\eta_{chillers}$ + 1.6
Pressure Independent Control Valve (~1200 GPM)	$\eta_{chillers}$ +$\eta_{chilled\ pump\text{-}1}$ + $\eta_{chilled\ pump\text{-}2}$
Chiller Setpoint	$\eta_{chillers}$
	5.88+η_{more}

References

1. L. Xie, K. Shan, H. Tang, S. Wang, Adv. Appl. Energy **18**, 100220 (2025).
2. E. Dulce-Chamorro, F. J. Martinez-de-Pison, J. Build. Eng. **43**, 102839 (2021).
3. S. Xing, J. Zhang, S. Li, J. Gao, H. Guan, Appl. Energy **376**, 124208 (2024).
4. Z. D. Tsai, C. S. Chen, MEDSI'**25**, 321 (2025).

Exploring the Dynamic Structural Evolution of Materials: TPS 20A Two-Dimensional X-ray Diffraction Beamline

Contemporary technology has evolved rapidly on the back of a solid understanding of material properties at the atomic level. Whether developing next-generation batteries, high-performance catalysts, or novel quantum materials, their properties such as conductivity, magnetism, thermal stability, and reactivity are governed by their internal crystal structures. However, in real-world applications, materials operate in complex environments involving heat, pressure, electricity, or gas adsorption. Consequently, modern materials science has shifted from merely identifying "static structures" to exploring the "dynamic evolution" of materials, such as how they undergo phase transitions, lattice distortions, or reconstruction under external stimuli.

To capture these dynamic processes under real-world operating conditions, the selection of appropriate experimental techniques is critical. Powder X-ray Diffraction has emerged as the preferred method for observing structural evolution under working conditions owing to its flexible sample preparation and compatibility with various environmental chambers. In this regard, the **TPS 20A** beamline was specifically designed to serve as a high-throughput platform with excellent temporal resolution. It allows researchers to continuously monitor structural evolution and capture transient phase transitions, thereby revealing the underlying kinetics and reaction mechanisms of functional materials.

The **TPS 20A** beamline uses a bending magnet source, delivering tunable X-ray energy of 8–30 keV. When using an Si (111) crystal monochromator, the energy resolution ($\Delta E/E$) reaches 2×10^{-4}, ensuring superior spectral quality. The photon flux at 10 keV is approximately 6×10^{11} photons/s, significantly exceeding that of the **TLS 01C2** beamline. This high flux is crucial for improving diffraction signal quality and dramatically reducing data acquisition time. The optical system has been optimized to provide a focused spot size of approximately 300 μm × 300 μm at the sample position, ensuring sufficient flux density and sampling volume.

The configuration of the endstation is illustrated in **Fig. 1**. This design balances the needs for "high-throughput screening" and "high-precision control". For large-scale powder analysis, the station features an automatic capillary alignment system paired with a robotic arm, allowing for fully automated sample exchange and maximizing data

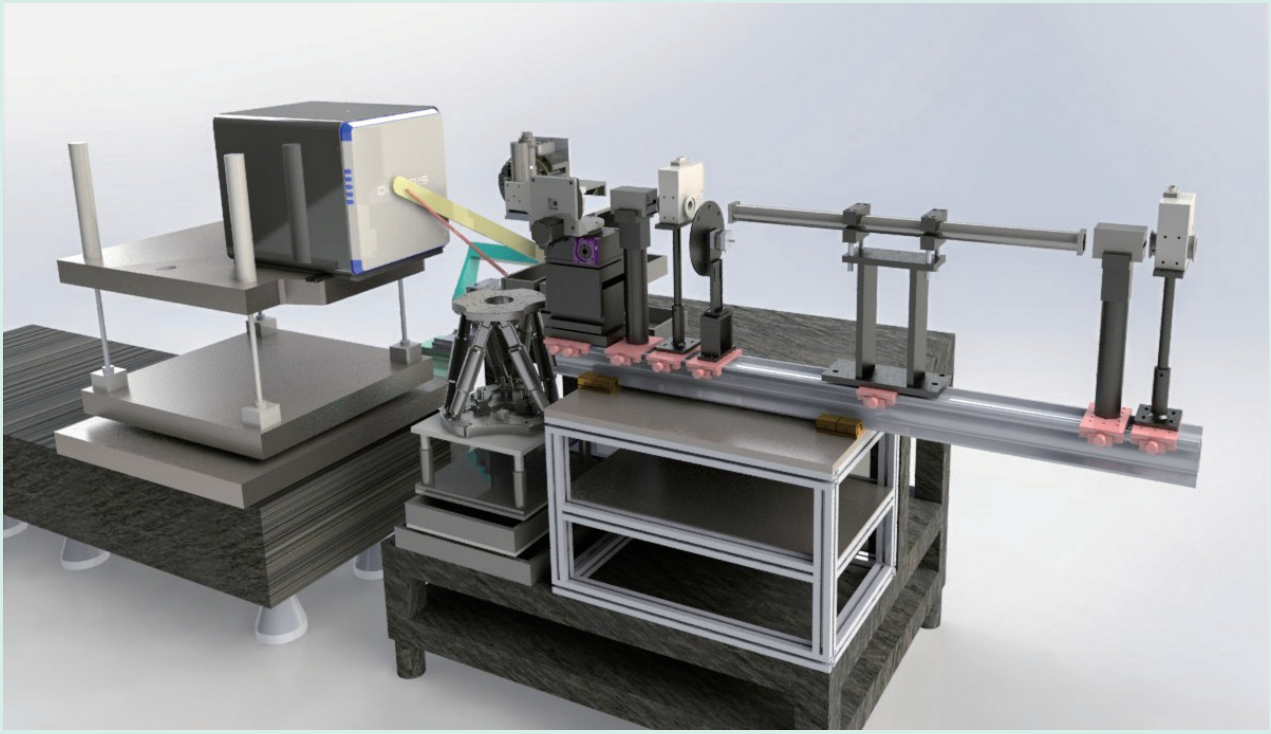

Fig. 1: Schematic diagram of **TPS 20A** endstation. The layout illustrates the arrangement of the Eiger2 S 16M detector, six-axis hexapod sample stage, and optical path configuration.

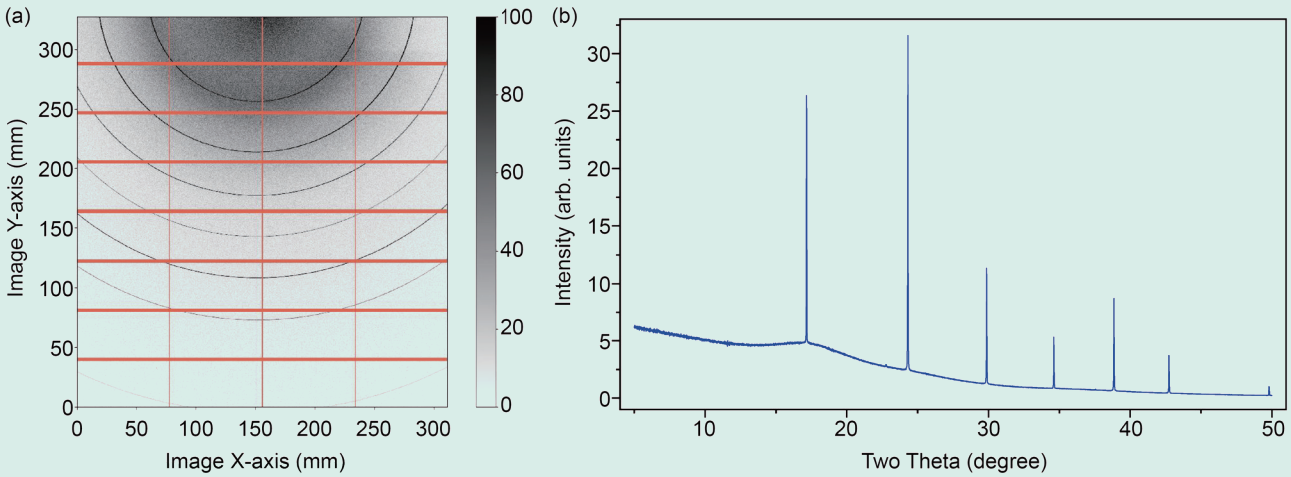

Fig. 2: Preliminary commissioning results at **TPS 20A**. (a) Two-dimensional powder diffraction pattern of a LaB6 standard, showing very low background noise. (b) Corresponding integrated intensity versus 2θ profile. Experimental conditions: Sample-to-detector distance of approximately 300 mm, covering a 2θ range of approximately 50°.

collection efficiency. For non-standard samples such as thin films, planar devices, or *in-situ* reaction chambers, a high-precision six-axis hexapod positioning stage is used. Unlike traditional stacked linear motors, the hexapod uses a parallel kinematic structure to provide exceptional stiffness and positioning accuracy across six degrees of freedom (X, Y, Z, pitch, roll, yaw). This capability is crucial for grazing incidence X-ray diffraction, where precise angular alignment is critical. Furthermore, the high load capacity of the hexapod allows it to stably support heavy *in-situ* equipment while maintaining micron-level stability.

To cater to diverse research needs, **TPS 20A** is equipped with comprehensive *in-situ* environmental equipment, including a high-temperature heat gun, low-temperature liquid nitrogen cryostream, potentiostat for electrochemical studies, and gas loading system. This versatility allows users from various fields to select environmental conditions appropriate for their specific experimental requirements. The detection system utilizes an Eiger2 S 16M photon-counting detector, which features a large active area (327.8 × 311.2 mm^2) and high pixel resolution (75 × 75 μm^2). These features help overcome the limitations of traditional image plates, such as slow readout and high noise, thereby significantly improving efficiency and dynamic range.

The hardware construction of **TPS 20A** is complete, and the beamline is undergoing commissioning with excellent preliminary results. Recent validation tests were performed using a LaB6 standard. With a sample-to-detector distance of approximately 300 mm, the system successfully collected diffraction signals covering a 2θ angle of approximately 50°. **Figure 2** shows the collected two-dimensional (2D) diffraction pattern and the corresponding integrated one-dimensional profile. The 2D pattern exhibits extremely low background and an exceptional signal-to-noise ratio. Compared to the image plate system at **TLS 01C2**, **TPS 20A** provides superior data quality and significantly shorter acquisition times, highlighting the advantages of photon-counting technology. Moreover, commissioning confirmed the flexibility of the detector stage, which allows users to adjust the detector position (centered or off-centered) and distance (closer to or farther from the sample) to optimize angular resolution and coverage according to experimental needs.

Looking forward, NSRRC's powder diffraction facilities will follow a strategic division of labor: **TPS 19A** will focus on high-resolution structural analysis, while **TPS 20A** will support experiments requiring longer reaction times and complex setups. Users of the existing **TLS 01C2** beamline will gradually be transitioned to **TPS 20A**, where they will benefit from more convenient and superior experimental facilities. During this transitional phase, the team will continue commissioning tasks, such as system integration, optimization, and testing various experiment types to ensure optimal beamline performance. **TPS 20A** is scheduled to open for general user proposals in the first quarter of 2026. In this initial phase, 20% of the beamtime will be allocated to general users. This facility is expected to be a powerful tool for the materials research community, facilitating deep exploration of functional materials, energy storage systems, and frontier physical properties. (Reported by Yen-Chung Lai)

Attenuator Design at TPS and SPring-8 12B2

Attenuators are commonly used to decrease the power of a light source and prevent damage to detector sensors and other optical components. For different beamlines and attenuation requirements, the primary challenge in this work is designing the **TPS 31A** attenuator.

The **TPS 31A** insertion device is a wiggler, and the white-beam size is 25 mm × 50 mm. The radiated power in white-beam operation mode is 1000 W, necessitating the use of an attenuator to absorb excess beam power. The **TPS 31A** attenuator is equipped with 12 foil carriers. The clear aperture is 46 mm × 56 mm, accommodating the beam in different operation modes. The system vacuum level reaches 1×10^{-7} mbar, and the cooling capacity exceeds 1000 W.

To address the thermal dissipation issue, this project employs a magnetic-coupling-type attenuator system with foil-carrier cooling through the side chamber walls, without introducing water feedthroughs into the vacuum chamber. In double-crystal monochromator (DCM) and double multilayer monochromator (DMM) modes, the **TPS 31A** beam's vertical position shifts. The foil window of the attenuator is therefore designed to be 56 mm (H) × 46 mm (V), allowing all operation modes (DCM, DMM, and white-beam mode) to pass through the attenuator. The foil carrier design is shown in **Fig. 1**.

The ball-bearing slide assembly uses six ball bearings, each lubricated with a fluoropolymer coating. With this configuration, the system can achieve a vacuum pressure of 1×10^{-7} mbar. If required, the ball bearings can be replaced with high-vacuum types, enabling the attenuator system to reach a pressure of 1×10^{-12} mbar. The pneumatic actuator provides 100 mm of travel and moves the outer chamber to position the magnet, thereby driving the foil carrier inside the vacuum chamber. The magnetic drive consists of two neodymium magnets. The frame and foil clamp are fabricated from 6061 aluminum alloy.

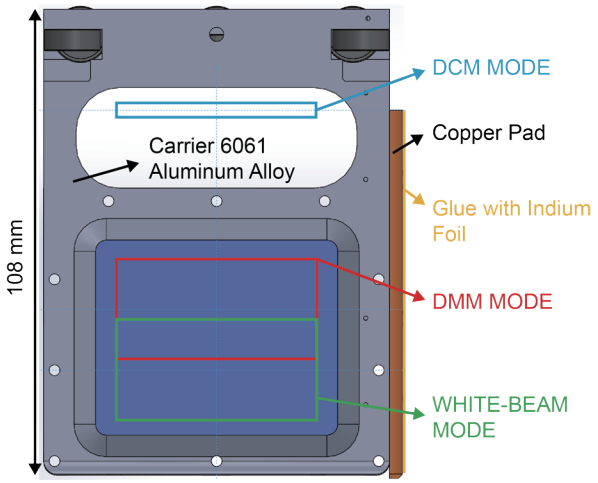

Fig. 1: Diagram of the foil carrier and beam footprint of the foil carrier in different operation modes: (1) DCM mode, (2) DMM mode, and (3) white-beam mode.

Increasing the absorption foil size helps reduce the maximum temperature in the foil and increases the contact area between the foil and the foil carrier. A copper contact pad interfaces the foil carrier with the cooling wall. The contact pad area is 87 mm × 23 mm, and this large contact area enhances heat transfer to the cooling wall. The thermal transfer path is from the foil to the carrier frame, then to the copper pad, glue, indium foil, vacuum chamber wall, and finally to the water-cooling plate.

TPS 31A is one of the most powerful projection X-ray microscope beamlines in the world. The high photon flux makes heat management a critical issue. In this work, a previous magnetic-coupling-type attenuator design, which lacked an integrated cooling system,[1–3] is improved by incorporating an efficient thermal path from the absorption foil to a water-cooled pad outside the vacuum chamber. As a result, the attenuator system remains compact, while the large absorption foil and foil carrier dimensions reduce both the thermal load density and the maximum system temperature. The **TPS 31A** attenuator system installed on the beamline is shown in **Fig. 2**.

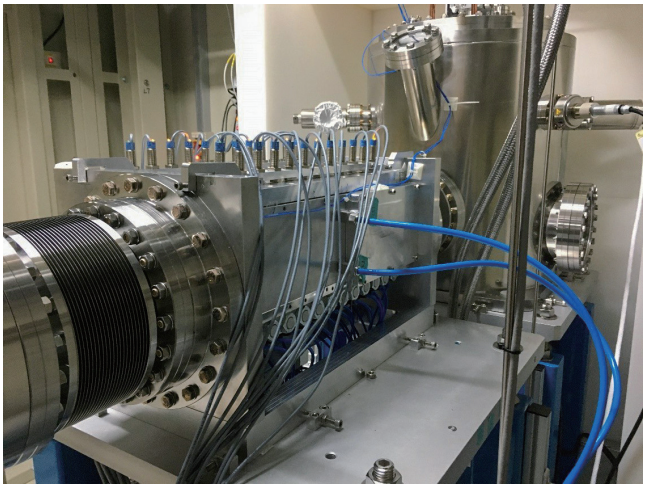

Fig. 2: Attenuator system installed on the **TPS 31A** beamline.

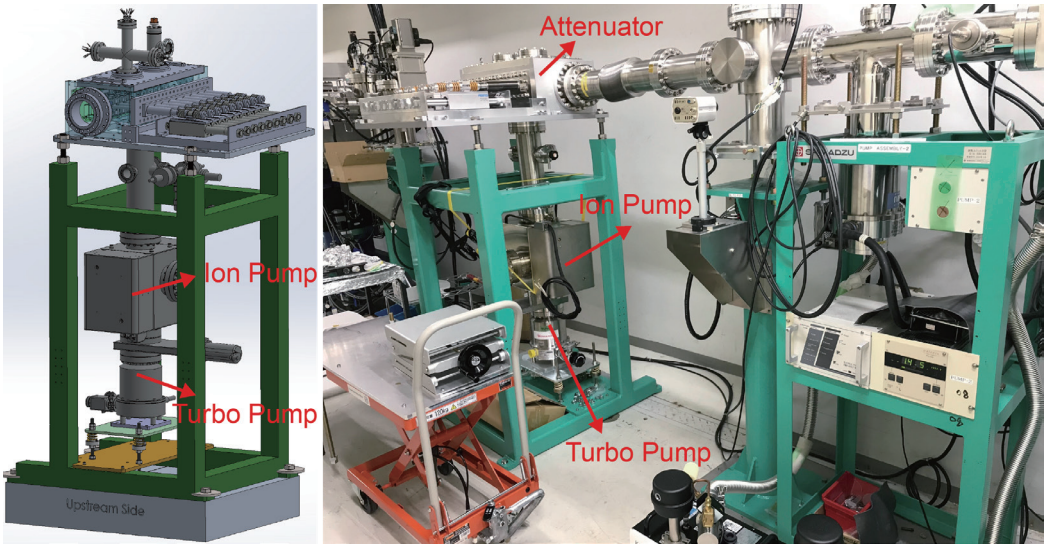

Fig. 3: The attenuator system installed in the SPring-8-II **BL12B2** beamline.

The light source for the **BL12B2** beamline at SPring-8-II is a bending magnet. This beamline enables X-ray absorption spectroscopy, high-resolution X-ray scattering, protein crystallography, and micro-beam scattering experiments. For the planned upgrade of **BL12B2**, an attenuator with nine filters has been designed. The filters are cooled through the chamber wall.

Each filter carrier is designed to absorb up to 100 W while keeping the maximum carrier temperature below 75 °C when the chamber wall temperature is 25 °C. The attenuator also functions as a pumping station and includes a 6-inch port that accommodates both an ion pump and a turbomolecular pump. The attenuator filters are driven by a pneumatic actuator, which positions each filter either in the beam path or in a cooling position. This attenuator was installed on the **BL12B2** beamline at SPring-8-II in April 2025.

The attenuator body is fabricated from 6061 aluminum alloy, which provides high thermal conductivity. The filter carriers are also made from 6061 aluminum alloy. When the filter foil absorbs energy from the light source, the filter carrier effectively dissipates heat and limits the temperature rise. The carrier clamps the foil and conducts heat to a copper pad, while the aluminum chamber wall provides additional cooling. On the outside of the chamber, a mini-channel fin water-cooling plate is attached. This plate incorporates rectangular mini-channels with a width of approximately 240 μm.

At a flow rate of 3.7 L/min (1 gallon/min), the pressure drop across the mini-channel plate is 5.998 kPa. Cooling water circulates through the plate, which is bolted to the chamber wall to improve heat dissipation. At the bottom of the attenuator, a 6 inch ConFlat flange is installed, providing the interface for both the ion pump and the turbo-molecular pump to maintain the beamline vacuum level. The overall attenuator system layout for **BL12B2** is shown in **Fig. 3**. (Reported by Ming-Ying Hsu)

References

1. M. Grujicic, C. L. Zhao, E. C. Dusel, Appl. Surf. Sci. **246**, 290 (2005).
2. J. H. Lienhard IV, J. H. Lienhard V, A Heat Transfer Textbook, New York: Dover (2019).
3. F. H. Milanez, J. R. Culham, M. M. Yovanovich, J. Thermophys. Heat Tr. **17**, 534 (2003).

Industrial Applications at the NSRRC (2024–2025)

Through advanced synchrotron capabilities, industry-dedicated infrastructure, expert scientific partnerships, and flexible industrial access models, the NSRRC continues to accelerate industrial innovation and strengthen Taiwan's global technological competitiveness.

Strategic Context & Vision
Taiwan's leadership in high-technology manufacturing depends on advanced analytical infrastructure to support rapid innovation. In this context, the NSRRC has strengthened its industrial engagement strategy over the past decade, positioning itself as a national R&D partner rather than solely an academic research facility. The establishment of the Industry Application Division marked a significant step toward integrating industrial applications within the NSRRC's mission.

By serving as a structured interface between synchrotron science and enterprise R&D teams, the NSRRC enables industry to access advanced characterization tools to address complex technical challenges. The focus includes semiconductors, energy storage, advanced materials, metallurgy, biomedical technologies, and precision devices—sectors central to Taiwan's economic development and global competitiveness.

In recognition of sustained efforts in strategic industrial engagement and innovation management, the NSRRC received the 2024 Technology Management Award (Academic and Research Team Category) from the Chinese Society for Management of Technology (中華民國科技管理獎). The award acknowledges the division's exceptional planning, promotion, and execution of the Industrial Application Service Platforms for Synchrotron Radiation Facility.

Industrial Access and Partnership Models
The NSRRC offers several engagement pathways tailored to industrial needs. Companies can access beamlines under proprietary arrangements that ensure confidentiality and intellectual property protection. Collaborative frameworks also enable beamline scientists and company engineers to jointly design experimental strategies and analytical methodologies.

Each major industrial sector is supported by dedicated project managers who cultivate long-term working relationships with corporate R&D divisions. This sector-specific approach enables the NSRRC to anticipate recurring technical challenges and provide targeted solutions efficiently. Beyond direct corporate engagement, the NSRRC collaborates with universities and analytical service providers to further expand industrial access to synchrotron capabilities.

Infrastructure Enabling Industrial Innovation
The NSRRC operates two synchrotron facilities, the Taiwan Light Source (TLS) and the Taiwan Photon Source (TPS), offering complementary high-brilliance X-ray capabilities. These facilities support advanced diffraction, scattering, spectroscopy, and imaging techniques essential for structural and chemical analysis across a wide range of materials systems.

The industrially dedicated **TLS 07A1** beamline has consistently addressed the majority (approximately 70%) of industrial analytical demands through integrated X-ray diffraction (XRD), X-ray scattering (XAS), and wide-angle X-ray scattering (WAXS) capabilities. As operational emphasis transitions toward TPS, a next-generation industrial beamline, **TPS 12A**, is being developed to incorporate advanced automation, high-throughput workflows, and AI-assisted data acquisition and analysis. This upgrade demonstrates the NSRRC's commitment to improving responsiveness, reproducibility, and operational efficiency for industrial users.

Accelerating Industrial Decision-Making
A key advantage of synchrotron-based analysis is its speed, sensitivity, and reliability. Compared with conventional laboratory instruments, synchrotron radiation enables rapid acquisition of statistically robust data, even for complex or low-signal systems.

This capability leads to shorter development cycles. Materials can be screened efficiently, structural transformations monitored in real time, and failure mechanisms identified at early stages. As a result, companies can make informed design and process decisions more quickly, reducing technical risk and optimizing resource allocation.

Key Industrial Domains and Impacts
1. Semiconductor Technologies
Taiwan's semiconductor ecosystem benefits significantly from its close geographic and technical integration with the NSRRC. Long-term collaborations have enabled semiconductor manufacturers to apply advanced techniques such as grazing-incidence diffraction and X-ray absorption spectroscopy to investigate nanoscale interfaces and ultra-thin dielectric layers.

Synchrotron-enabled diagnostics have clarified defect-related leakage mechanisms in high-k materials, contributing to performance optimization in advanced nano-scale chips. These sustained partnerships demonstrate how large-scale research infrastructure can be effectively embedded within industrial innovation pipelines.

In addition, synchrotron-based metrology has supported domestic development of extreme ultraviolet lithography-related materials and processes, providing benchmark characterization tools that reinforce Taiwan's leadership in advanced semiconductor manufacturing.

2. Energy Storage and Lithium-Ion Batteries
Energy storage is another area of ongoing industrial collaboration. *Operando* and *in situ* X-ray techniques have been used to monitor electrochemical processes in lithium-ion batteries, revealing phase transitions and interfacial evolution during charge–discharge cycling.

These structural insights have guided electrode material optimization, enhanced performance stability and supported patented technologies. Advanced battery systems informed by synchrotron analysis have been deployed in grid-scale energy storage and high-performance electric vehicles, demonstrating the practical impact of photon science on clean energy technologies.

3. Polymers and Carbon Fiber Materials
For polymer and fiber industries, small-angle X-ray scattering (SAXS) provides a critical understanding of mesoscale structural evolution. By analyzing crystallization kinetics and hierarchical organization, companies have enhanced the mechanical performance of recycled polymer-based materials, enabling entry into high-value international markets.

In carbon fiber development, micro-beam techniques have revealed structural heterogeneity within individual filaments, linking nanoscale architecture to macroscopic mechanical strength. These findings inform process optimization and support the scaling of production lines for aerospace-grade applications.

4. Sustainable Metallurgy
In response to carbon neutrality goals, the NSRRC participates in hydrogen-based metallurgy initiatives to reduce emissions in steel production. A high temperature (1800 °C), environmentally controlled experimental platform enables real-time *in situ* synchrotron radiation analysis using XRD, XAS, and X-ray imaging techniques to monitor the structural and chemical evolution during reduction reactions.

This infrastructure supports the development of cleaner and more sustainable metallurgical technologies, aligning with Taiwan's national net-zero carbon target for 2050.

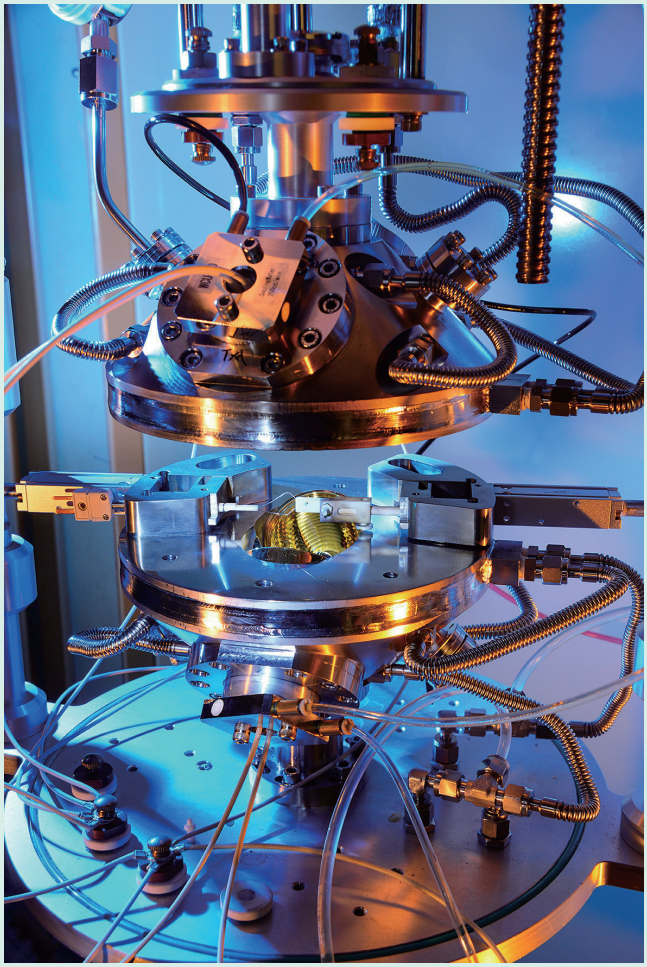

Fig. 1: A movable high-temperature (up to 1800 °C) *in situ* synchrotron platform adaptable to multiple beamlines, enabling real-time XRD, XAS, and X-ray imaging for hydrogen-based steelmaking research and low-carbon metallurgical technologies aligned with Taiwan's 2050 net-zero target.

5. Biomedical and Micro-Device Innovation
In the biomedical sector, integrated analytical platforms that combine fractionation techniques, light scattering, and X-ray methods enable detailed structural characterization of nanoparticle-based drug delivery systems. These insights support optimization of formulations for vaccines and therapeutic carriers.

The number of pharmaceutical users increased significantly in 2024 and 2025, driven by the adaptation of the bio-SAXS beamline **TPS 13A** for studies on drug delivery and carrier systems.

Technology transfer has also extended to microfabrication. Deep X-ray lithography processes developed at the NSRRC have enabled the production of compact spectrometer chips for portable diagnostics. This spectrometer chip technology has received national innovation awards and demonstrates strong commercial scalability, highlighting how synchrotron-based fabrication can catalyze start-up

growth and AI-enabled healthcare solutions.

6. Accelerator Technologies

The extensive experience accumulated by the NSRRC's accelerator divisions has enabled the provision of consultancy services to domestic hospitals and other synchrotron facilities in the design of high-quality magnet systems and vacuum infrastructure. In 2025, revenue from accelerator-related technologies contributed approximately 20% of total industrial income, reflecting the broader technological impact of the NSRRC beyond beamline applications.

Fig. 2: The mini-workshop on Analytical Advantages of Synchrotron Radiation Sources in Drug Delivery, held during the NSRRC 2025 User's Meeting. It attracted participants from academia and industry, highlighting NSRRC's bridging role.

Expertise as a Core Strength

Beyond advanced instrumentation, the NSRRC's scientific personnel are crucial to industrial success. Beamline scientists empower with experiment design, methodology development, and data interpretation, ensuring that analytical results become actionable industrial knowledge. This collaborative model builds trust, increases efficiency and supports long-term industrial partnerships.

Expanding Industrial Ecosystems

Industrial engagement has evolved from single-experiment interactions to programmatic, multi-year collaborations. The number of industrial commission cases increased from 39 in 2024 to 52 in 2025, reflecting rising annual revenue.

To further strengthen industry engagement and knowledge exchange, dedicated workshops were organized during the NSRRC 2025 User's Meeting, including the Extreme Ultraviolet Technology and Applications Workshop and a mini-workshop on the Analytical Advantages of Synchrotron Radiation Sources in Drug Delivery. In addition, "Propelled Toward Vega: Accelerating the Synthetic Fiber Industry's Next Step," presented at the Taipei Innotech Expo in October 2025, engaged approximately 100 visitors, including industry partners and the public. Together, these events attracted participants from industry, academia, and the public, reinforcing NSRRC's role as a bridge between scientific research and industrial implementation.

Outlook

The upcoming industrial beamline at the TPS, designed with integrated automation and AI-driven data workflows, marks the next milestone in enhancing industrial service capacity. Through ongoing infrastructure upgrades, strengthened collaborative networks, and expanded industry-focused support, the NSRRC is well positioned to deepen its impact on Taiwan's innovation ecosystem in the years ahead. (Reported by Mau-Tsu Tang)

Fig. 3: Presentation of "Propelled Toward Vega: Accelerating the Synthetic Fiber Industry's Next Step" at the October 2025 Taipei Innotech Expo. It attracted about 100 visitors, including industry partners and members of the public.